



HAL
open science

TransCom 3 inversion intercomparison: Impact of transport model errors on the interannual variability of regional CO₂ fluxes, 1988-2003

D. Baker, R. Law, K. Gurney, P. Rayner, P. Peylin, A. Denning, Philippe Bousquet, L. Bruhwiler, Y.-H. Chen, Philippe Ciais, et al.

► To cite this version:

D. Baker, R. Law, K. Gurney, P. Rayner, P. Peylin, et al.. TransCom 3 inversion intercomparison: Impact of transport model errors on the interannual variability of regional CO₂ fluxes, 1988-2003. *Global Biogeochemical Cycles*, 2006, 20 (1), pp.n/a-n/a. 10.1029/2004GB002439 . hal-02924875

HAL Id: hal-02924875

<https://hal.science/hal-02924875>

Submitted on 28 Oct 2020

HAL is a multi-disciplinary open access archive for the deposit and dissemination of scientific research documents, whether they are published or not. The documents may come from teaching and research institutions in France or abroad, or from public or private research centers.

L'archive ouverte pluridisciplinaire **HAL**, est destinée au dépôt et à la diffusion de documents scientifiques de niveau recherche, publiés ou non, émanant des établissements d'enseignement et de recherche français ou étrangers, des laboratoires publics ou privés.

TransCom 3 inversion intercomparison: Impact of transport model errors on the interannual variability of regional CO₂ fluxes, 1988–2003

D. F. Baker,^{1,2} R. M. Law,³ K. R. Gurney,^{4,5} P. Rayner,^{3,6} P. Peylin,⁷ A. S. Denning,⁴ P. Bousquet,⁷ L. Bruhwiler,⁸ Y.-H. Chen,⁹ P. Ciais,⁷ I. Y. Fung,¹⁰ M. Heimann,¹¹ J. John,¹⁰ T. Maki,¹² S. Maksyutov,¹³ K. Masarie,⁸ M. Prather,¹⁴ B. Pak,^{14,15} S. Taguchi,¹⁶ and Z. Zhu¹⁷

Received 28 December 2004; revised 23 August 2005; accepted 11 October 2005; published 7 January 2006.

[1] Monthly CO₂ fluxes are estimated across 1988–2003 for 22 emission regions using data from 78 CO₂ measurement sites. The same inversion (method, priors, data) is performed with 13 different atmospheric transport models, and the spread in the results is taken as a measure of transport model error. Interannual variability (IAV) in the winds is not modeled, so any IAV in the measurements is attributed to IAV in the fluxes. When both this transport error and the random estimation errors are considered, the flux IAV obtained is statistically significant at $P \leq 0.05$ when the fluxes are grouped into land and ocean components for three broad latitude bands, but is much less so when grouped into continents and basins. The transport errors have the largest impact in the extratropical northern latitudes. A third of the 22 emission regions have significant IAV, including the Tropical East Pacific (with physically plausible uptake/release across the 1997–2000 El Niño/La Niña) and Tropical Asia (with strong release in 1997/1998 coinciding with large-scale fires there). Most of the global IAV is attributed robustly to the tropical/southern land biosphere, including both the large release during the 1997/1998 El Niño and the post-Pinatubo uptake.

Citation: Baker, D. F., et al. (2006), TransCom 3 inversion intercomparison: Impact of transport model errors on the interannual variability of regional CO₂ fluxes, 1988–2003, *Global Biogeochem. Cycles*, 20, GB1002, doi:10.1029/2004GB002439.

1. Introduction

[2] The concentration of CO₂ in the atmosphere has been monitored continuously since 1958 [Keeling *et al.*, 1989] at a growing number of sites. When deseasonalized, these records show that global CO₂ levels have increased monotonically for the last 45 years, but at a rate that varies strongly from year to year. Two human activities that add

large amounts of carbon to the atmosphere are thought to be the main drivers of the increase: fossil fuel burning and deforestation. Comparing this anthropogenic input to the observed increase rate, it is found that about 55% of the input does not stay in the atmosphere, but is apparently taken up by sinks in the ocean and land biosphere. Since fossil fuel burning has increased relatively smoothly across this span, the large interannual swings in atmospheric CO₂

¹Program in Atmospheric and Oceanic Sciences, Princeton University, Princeton, New Jersey, USA.

²Now at Terrestrial Sciences Section, National Center for Atmospheric Research, Boulder, Colorado, USA.

³CSIRO Marine and Atmospheric Research, Aspendale, Victoria, Australia.

⁴Department of Atmospheric Science, Colorado State University, Fort Collins, Colorado, USA.

⁵Now at Department of Earth and Atmospheric Sciences and Department of Agronomy, Purdue University, West Lafayette, Indiana, USA.

⁶Now at Laboratoire des Sciences du Climat et de l'Environnement, Gif-sur-Yvette, France.

⁷Laboratoire des Sciences du Climat et de l'Environnement, Gif-sur-Yvette, France.

⁸Climate Monitoring and Diagnostics Laboratory, National Oceanic and Atmospheric Administration, Boulder, Colorado, USA.

⁹Department of Earth, Atmospheric and Planetary Science, Massachusetts Institute of Technology, Cambridge, Massachusetts, USA.

¹⁰Center for Atmospheric Sciences, University of California, Berkeley, California, USA.

¹¹Department of Biogeochemical Systems, Max-Planck-Institut für Biogeochemie, Jena, Germany.

¹²Quality Assurance Section, Atmospheric Environment Division, Observations Department, Japan Meteorological Agency, Chiyoda-ku, Tokyo, Japan.

¹³Institute for Global Change Research, Frontier Research Center for Global Change, Japan Agency for Marine-Earth Science and Technology, Yokohama, Japan.

¹⁴Department of Earth System Science, University of California, Irvine, California, USA.

¹⁵Now at CSIRO Marine and Atmospheric Research, Aspendale, Victoria, Australia.

¹⁶Global Environment Study Group, Research Institute of Environmental Management Technology, National Institute of Advanced Industrial Science and Technology, Ibaraki, Japan.

¹⁷Goddard Space Flight Center, Greenbelt, Maryland, USA.

growth rates are apparently caused by interannual variability (IAV) in these sinks, though IAV in the rates of deforestation and biomass burning may be also important [Langenfelds *et al.*, 2002]. It is important to understand these variations in order to gain insight into the processes underlying the CO₂ fluxes and how they might change in the future.

[3] Over recent years a number of groups have used various inversion methods to estimate the IAV of CO₂ sources and sinks from atmospheric concentration data [Rayner *et al.*, 1999; Law, 1999; Bousquet *et al.*, 2000; Baker, 2001; Piper *et al.*, 2001a, 2001b; Rödenbeck *et al.*, 2003]. These results are often similar when viewed as integrals across broad latitude bands, but differences between them become marked when fluxes are partitioned regionally inside these latitude bands. In general, it has been difficult to reconcile the inconsistencies between inversion results because of the different inversion methods, setups, and transport models used by each group [Peylin *et al.*, 2002]. The TransCom 3 project was designed specifically to assess how differences in atmospheric transport models affect CO₂ flux inversions.

[4] In the TransCom 3 project, CO₂ flux inversions have been performed in which the details of the method and setup were fixed and only the transport model (and for some models, the source of the winds) varied. The TransCom 3 project has evolved through a number of phases. The first phase focused on estimating 5-year mean sources for 22 regions for 1992–1996 with 16 different transport models (G02 [Gurney *et al.*, 2002]; G03 [Gurney *et al.*, 2003]). It was found that source uncertainty due to the use of different transport models was generally comparable to or smaller than the estimation uncertainties due to random errors in the limited CO₂ data available. The sensitivity of the results to the a priori flux uncertainties (G03) and to the choice of measurements and data errors used [Law *et al.*, 2003] was also examined.

[5] The second phase of TransCom 3 focused on estimating the mean seasonal cycle of sources across 1992–1996 (G04 [Gurney *et al.*, 2004]). A smaller set of 12 transport models, the ones submitting time-dependent response functions to the project, were examined. It was found that the 1 σ spread of estimated sources from the different models was larger than the estimated uncertainty in the northern extratropics but smaller than that uncertainty in tropical regions. The largest model spread occurred during the growing season for northern land regions.

[6] Here, in the third phase of the TransCom 3 project, we focus on the interannual variability of the CO₂ sources and sinks. We solve for monthly CO₂ sources for 1988–2003 for 22 regions using 13 different transport models (those from G04, plus one). We assess the sensitivity of the estimated IAV to the transport model used, and present the mean IAV obtained across all the models.

[7] In section 2, we describe the setup of the problem, outline the method, and specify how the flux interannual variability is calculated. In section 3, we present our results, starting with a brief comparison to previously published long-term mean fluxes, then focusing on the interannual variability of the fluxes. We use the standard deviation in the results across the models as a proxy for transport model

uncertainty, then discuss the significance of the flux IAV in light of these transport uncertainties and the random estimation uncertainties. In section 4, we compare our results to other published IAV results, discussing possible explanations for the differences. For the robust features of our inversion, we discuss physical mechanisms that may be driving the system. Finally, in section 5, we summarize our approach and results, and discuss the implications for future inversion strategies and network design.

2. Method

2.1. Estimation Method

[8] We use Bayesian synthesis inversion [Enting, 2002] to estimate CO₂ sources and their uncertainties given a set of atmospheric CO₂ concentration data and their uncertainties. The mathematical details of the Bayesian synthesis approach for the interannual case are given by Baker [1999, 2001]. Here we summarize the method and describe the values used for the required input parameters.

[9] We specify the fossil fuel burning source and solve for the natural sources from the ocean and land biosphere. The anthropogenic input from biomass burning and deforestation is not explicitly modeled in the inversion, so that the estimated net land flux includes the effect of biomass burning, as well as corrections to the assumed fossil fuel burning and the effects of any other nonmodeled processes over land (such as net fluxes from reservoirs, rivers, or coastal zones).

[10] Surface fluxes are estimated for 22 predefined emission regions (Figure 1) for each month across 1988–2003. For each region and month of the year, a prespecified flux pattern (normalized to 1 PgC yr⁻¹) is run forward through the transport model (1 month on, subsequent months off) to calculate its effect on atmospheric CO₂ concentrations at later times. These concentration “footprints” are sampled at the measurement locations to obtain the columns of a matrix \mathbf{H} relating the modeled concentrations $\mathbf{c}_{\text{model}}$ at the measurement sites to regional flux magnitudes \mathbf{x} as in $\mathbf{c}_{\text{model}} = \mathbf{c}_{\text{fwd}} + \mathbf{H}\mathbf{x}$. Concentrations \mathbf{c}_{fwd} , generated from transport model runs using fine-scale prior fluxes \mathbf{f}_{fwd} (described below), are presubtracted from measured concentrations \mathbf{c}_{obs} . The inversion estimates regional flux magnitudes $\hat{\mathbf{x}}$, which may be thought of as coarse-scale corrections to \mathbf{f}_{fwd} ; the fine-scale corrections to \mathbf{f}_{fwd} are given by $\mathbf{F}\hat{\mathbf{x}}$, where the columns of \mathbf{F} are given by the prespecified flux patterns inside each region/month used to generate \mathbf{H} . Both \mathbf{c} and \mathbf{x} contain monthly average values for each month in the measurement span (78 concentrations and 22 fluxes, respectively), while \mathbf{x} also contains fluxes for 35 months preceding the first measurements plus a single concentration offset for the full span.

[11] The optimal $\hat{\mathbf{x}}$ is solved for by minimizing a Bayesian least squares cost function,

$$J = (\mathbf{c}_{\text{obs}} - \mathbf{c}_{\text{fwd}} - \mathbf{H}\mathbf{x})^T \mathbf{R}^{-1} (\mathbf{c}_{\text{obs}} - \mathbf{c}_{\text{fwd}} - \mathbf{H}\mathbf{x}) + (\mathbf{x}_0 - \mathbf{x})^T \mathbf{P}_0^{-1} (\mathbf{x}_0 - \mathbf{x}), \quad (1)$$

where $\mathbf{c}_{\text{obs}} - \mathbf{c}_{\text{fwd}}$ are measurement mismatches between the true observations and the concentrations given by the fine-scale prior fluxes \mathbf{f}_{fwd} , \mathbf{R} is the covariance matrix for the

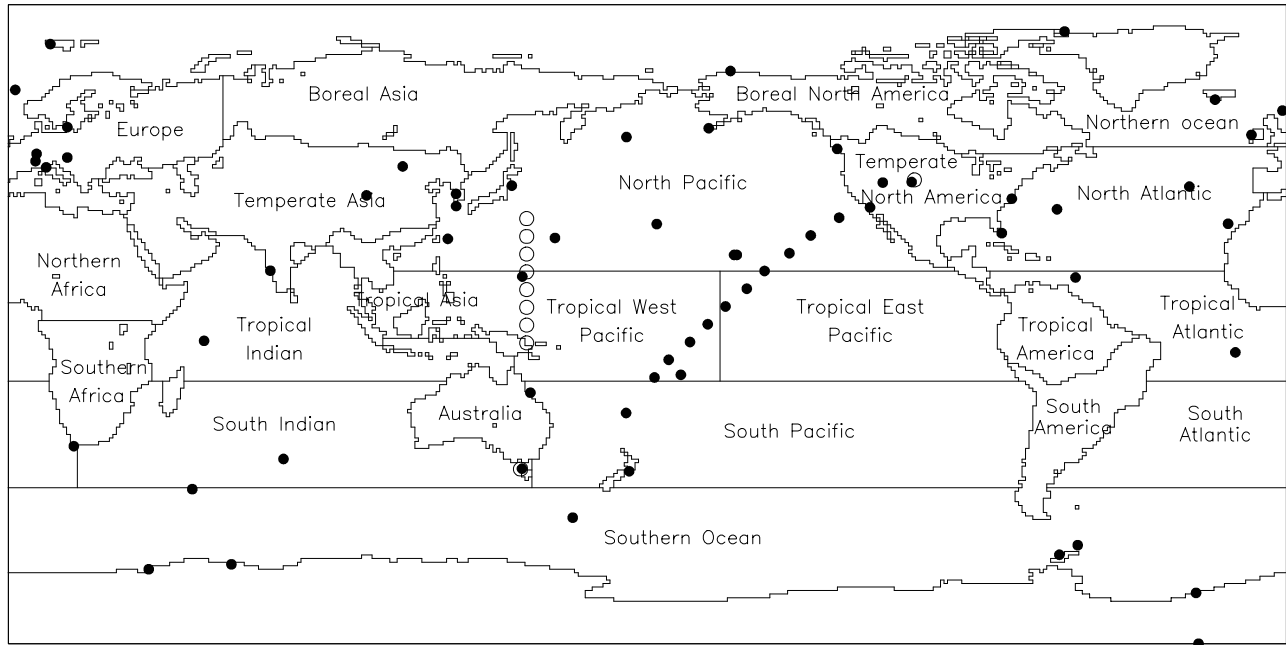


Figure 1. A map of the 22 emission regions and 78 CO₂ measurement locations used in this study. Solid circles indicate surface measurements, and open circles indicate aircraft measurements.

errors in $\mathbf{c}_{\text{obs}} - \mathbf{c}_{\text{fwd}}$, \mathbf{x}_0 is an a priori estimate of the flux magnitudes, and \mathbf{P}_0 is the covariance matrix for the errors in \mathbf{x}_0 .

[12] The a posteriori regional flux estimate $\hat{\mathbf{x}}$ may be solved for analytically as

$$\hat{\mathbf{x}} = (\mathbf{H}^T \mathbf{R}^{-1} \mathbf{H} + \mathbf{P}_0^{-1})^{-1} (\mathbf{H}^T \mathbf{R}^{-1} (\mathbf{c}_{\text{obs}} - \mathbf{c}_{\text{fwd}}) + \mathbf{P}_0^{-1} \mathbf{x}_0) \quad (2)$$

and the a posteriori covariance \mathbf{P} (quantifying the “estimation uncertainty” in $\hat{\mathbf{x}}$) by

$$\mathbf{P}^{-1} = \mathbf{P}_0^{-1} + \mathbf{H}^T \mathbf{R}^{-1} \mathbf{H}. \quad (3)$$

The estimate is obtained numerically using an SVD-based approach [Baker, 2001] that allows the conditioning of the inversion to be easily assessed.

2.2. Transport Basis Functions and Presubtracted Tracers

[13] The prespecified flux patterns in \mathbf{F} used in generating \mathbf{H} for the land regions are set to annual mean net primary productivity (NPP) patterns from the CASA land biosphere model [Randerson *et al.*, 1997], while those for the ocean regions are spatially constant. The model run for each month-long pulse is carried out for 35 months past the emission month; subsequent months are approximated using exponential decay to the fully mixed state (with $\tau = 24$ months). A total of 264 response functions (22 regions \times 12 emission months) was produced in this manner. In all these transport model runs, as well as the ones to generate \mathbf{c}_{fwd} , a single year’s set of winds and vertical mixing parameters was used repeatedly for each year in the runs. When filling the columns of \mathbf{H} with the sampled response functions, this allows us to

use the runs for each emission month repeatedly, once for each emission year estimated. Not modeling the IAV in the transport fields in this way reduced the required model run time by a factor 19 (the number of years estimated), allowing more transport models to be used in our study. However, because we used transport fields not matched to the actual transport for each year in our span, our transport errors are best thought of as those suffered in inversions done with models driven by “climatological” winds.

[14] By not modeling the IAV in the transport, we assume all the IAV in the CO₂ measurements is due entirely to IAV in the sources and sinks. The adequacy of this approximation is supported by the results of Dargaville *et al.* [2000] and Rödenbeck *et al.* [2003]. Another study has found that not modeling the transport IAV causes standard errors of only about 0.2 PgC yr⁻¹ in an interannual CO₂ flux inversion similar to ours (Prabir Patra, personal communication, April 2005). However, there are suggestions these errors may be larger [e.g., Murayama *et al.*, 2004]. Clearly, to obtain the most precise flux results, the true winds and vertical mixing should be modeled as well as possible, by using reanalyzed meteorological fields to drive the transport model. When computational resources permit it, a study of the sort done here should be carried out using only transport models driven by such fields in order to obtain more precise transport error estimates.

[15] The fine-scale prior fluxes \mathbf{f}_{fwd} used to generate \mathbf{c}_{fwd} are composed of the sum of three terms: seasonally varying net ecosystem exchange (NEE = heterotrophic respiration – NPP) from the CASA land biosphere model [Randerson *et al.*, 1997]; seasonally varying air-sea CO₂ fluxes [Takahashi *et al.*, 1999]; and interannually varying fossil fuel fluxes. The spatial pattern of the fossil fuel term is obtained by interpolating in time between unitized versions of the 1990 field of

Table 1. Annual Fossil Fuel Burning Assumed, Taken as the Sum of National Fossil Fuel Emissions, CO₂ From Cement Production, and a Bunker Fuels Term Averaging 0.09 PgC yr⁻¹ Across 1988–2003^a

Year	Fossil Fuel, PgC yr ⁻¹
1988	5.93
1989	6.04
1990	6.11
1991	6.19
1992	6.07
1993	6.08
1994	6.24
1995	6.38
1996	6.53
1997	6.63
1998	6.62
1999	6.67
2000	6.82
2001	6.92
2002	7.00
2003	7.00

^aSum of national fossil fuel emissions is from *Energy Information Administration* [2002]. Cement production is from *Marland et al.* [2003].

Andres et al. [1996] and the 1995 field of A. L. Brenkert (Carbon dioxide emission estimates from fossil-fuel burning, hydraulic cement production, and gas flaring for 1995 on a one degree grid cell basis, 1998, available at <http://cdiac.esd.ornl.gov/ndps/ndp058a.html>). To obtain the three terms, four global tracers (CASA NEE, Takahashi ocean, 1990 and 1995 fossil fuel) are run through the transport model with the fluxes turned on for one year and turned off for two more years; subsequent years are given by the same exponential decay described above. Interannual concentration time series are then built up by applying these single-year response functions to a priori emissions for each year in the span and for a spin-up period of several years before; the annual land and ocean flux totals were constant from year to year, while the annual fossil fuel fluxes varied according to the values in Table 1. As the oceanic and fossil fuel fluxes are not annually balanced, \mathbf{c}_{fwd} contains an interannual trend that when subtracted from the trend in \mathbf{c}_{obs} , allows the inversion to constrain the total net land/ocean flux without any additional constraints being applied.

2.3. Priors and Measurements

[16] The same seasonally varying a priori regional flux magnitudes \mathbf{x}_0 used in G04 have been used here (see the auxiliary material¹). These regionally-integrated corrections to \mathbf{f}_{fwd} include seasonally varying deforestation and re-growth estimates not contained in the annually balanced CASA NEE fields. Table 3 in section 3.1 gives the annual mean of \mathbf{x}_0 , with the contribution of \mathbf{f}_{fwd} added back on.

[17] Correlations between the errors for the different regions and months in \mathbf{x}_0 are neglected here, so that the a priori error covariance \mathbf{P}_0 is diagonal. Our a priori uncertainties are loose enough that neglecting these correlations should have a minimal impact on our results. The 1σ a priori regional flux uncertainties composing the main diagonal of

\mathbf{P}_0 are the seasonally varying ones of G04 for the land regions, and a constant $\sigma_{\text{ocn}} = \sqrt{(0.50 \text{ PgC yr}^{-1})^2 + \sigma_{L1}^2}$ for the ocean regions, where σ_{L1} are the annual mean a priori uncertainties used in G03. The monthly varying a priori uncertainties used here are given in the auxiliary material, while annual uncertainties computed from these are given in Table 4 in section 3.1.

[18] We use CO₂ data from 78 time series from *GLOBALVIEW-CO₂* [2004] (locations given in Figure 1; see auxiliary material for further details). GLOBALVIEW is a data product in which quality-controlled flask and continuous CO₂ observations are fitted to give 48 synchronous CO₂ values per year, with an extrapolation procedure used to fill gaps in the observation records [*Masarie and Tans*, 1995]. Frequencies with features shorter than 40 days are filtered out by the fitting procedure, yielding time series more easily matched by models driven by climatological winds, such as ours. We have selected sites at which valid observations are available for at least 68% of the time across 1991–2000. We generate the monthly concentrations in \mathbf{c}_{obs} by averaging each four pseudo-weekly GLOBALVIEW values per month. We use the extrapolated data from GLOBALVIEW where data are missing, and increase the data uncertainties at those times to reflect the errors in the extrapolation procedure.

[19] In Appendix A, we describe the measurement uncertainties used in \mathbf{R} . These vary seasonally and interannually to account for changes in measurement density, while extra errors have been added to some sites to account for site-specific modeling inadequacies. All measurements are considered independent, so that matrix \mathbf{R} is diagonal, with σ_{data}^2 from (A1) on the diagonal (see the auxiliary material for values). We have deliberately left certain spatially redundant sites out of the inversion (i.e., choosing only a single time series at any given measurement location) to reduce the errors introduced by this no-correlation assumption. Our averaging period (1 month) is long enough to keep time correlations to a minimum; we would expect that it would be more important to model these correlations when solving at timescales shorter than a week, where synoptic-scale transport errors would become more of a factor.

2.4. Computation of the Long-Term Mean, Interannual Variability, and Seasonal Cycle of the Fluxes

[20] Equation (2) yields flux magnitude estimates \mathbf{x}^{mon} for each region and month in the 1988–2003 measurement span; this is done separately for each transport model using that model's \mathbf{H} and \mathbf{c}_{fwd} . Thirteen models submitting time-dependent response functions to the intercomparison (Table 2) have been used here (the 12 from G04, plus PCTM). Figure 2a gives an example of what the flux results look like for one region, Europe, for inversions done with the 13 different models. For a clearer view of the IAV in the result, it is useful to remove the seasonal cycle (Figure 2b). We do this here with a compact running annual mean, centered on the month in question,

$$\mathbf{x}_i^{\text{deseas}} = \left(\sum_{j=i-6}^{i+5} w_j \mathbf{x}_j^{\text{mon}} + \sum_{j=i-5}^{i+6} w_j \mathbf{x}_j^{\text{mon}} \right) / 2, \quad (4)$$

¹Auxiliary material is available at <ftp://ftp.agu.org/apend/gb/2004GB002439>.

Table 2. Description of the 13 Atmospheric Transport Models Used

Model	Modelers	Wind Frequency, Source, and Year	Resolution, Longitude × Latitude × Levels
CSU	Gurney	online	5° × 4° × 17 sigma
GCTM	Baker	6 hour ZODIAC GCM	(256 km) ² × 18 sigma
JMA	Maki	6 hour JMA, 1997	2.5° × 2.5° × 32 hybrid
MATCH:CCM3	Bruhwieler	6 hour NCAR CCM3	2.8° × 2.8° × 28 hybrid
MATCH:MACCM3	Law	6 hour MACCM3	5.6° × 2.8° × 24 hybrid
MATCH:NCEP	Chen	6 hour NCEP, 1990	2.8° × 2.8° × 28 hybrid
NIES	Maksyutov	12 hour ECMWF, 1997	2.5° × 2.5° × 15 sigma
NIRE	Taguchi	6 hour ECMWF, 1995	2.5° × 2.5° × 15 hybrid
PCTM	Zhu	6 hour GEOS-DAS3, 1987	2.0° × 2.5° × 25 hybrid
TM2	Bousquet, Peylin	12 hour ECMWF, 1990	7.5° × 7.5° × 9 sigma
TM3	Heimann	6 hour ECMWF, 1990	5° × 4° × 19 hybrid
UCB	Fung, John	1 hour GISS GCM II'	5° × 4° × 9 sigma
UCI	Pak, Prather	3 hour GISS GCM II'	5° × 4° × 9 sigma

where w_j are weights that account for the length of each calendar month, and where we use the notation $\mathbf{x}_j^{\text{mon}}$ to refer to the subvector of \mathbf{x}^{mon} for month j . The time variability obtained using the different models is similar, but each model seems to have its own characteristic offset. These offsets may be removed by subtracting off the long-term means for each model, given by

$$\mathbf{x}^{\text{mean}} = \frac{1}{N} \sum_{i=1}^N \mathbf{x}_i^{\text{deseas}} \quad (5)$$

so that only a zero-mean IAV, \mathbf{x}^{IAV} , remains (Figure 2c). With the long-term means removed, the similarity in the IAV between the models becomes much clearer.

[21] Using equations (4) and (5) above, we split our a posteriori monthly regional flux estimate into three parts, the long-term mean, the zero-mean interannual variability, and a time-varying seasonal cycle (zero-mean over any 12 months), as

$$\mathbf{x}_i^{\text{mon}} = \mathbf{x}_i^{\text{deseas}} + \mathbf{x}_i^{\text{seas}} = \mathbf{E}\mathbf{x}^{\text{mean}} + \mathbf{x}_i^{\text{IAV}} + \mathbf{x}_i^{\text{seas}}, \quad (6)$$

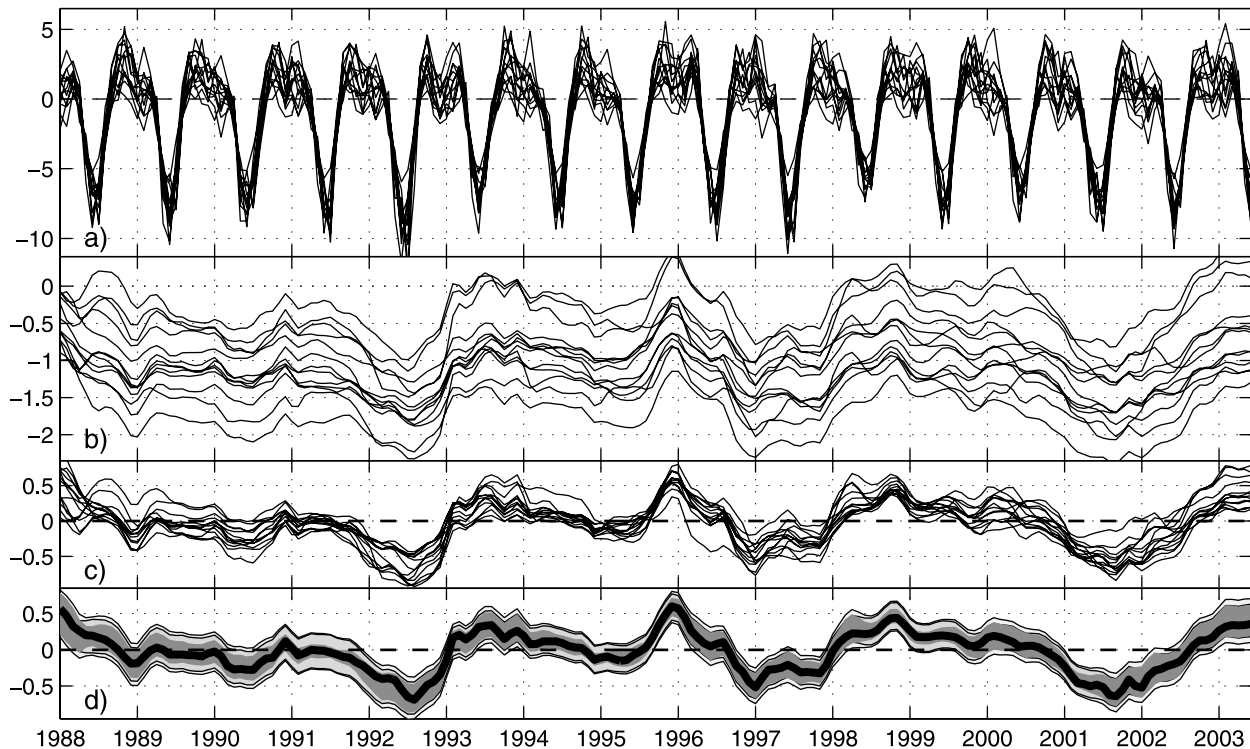


Figure 2. (a) Monthly flux estimates \mathbf{x}^{mon} (PgC yr⁻¹) obtained for Europe using the 13 different transport models; (b) the deseasonalized flux time series $\mathbf{x}^{\text{deseas}}$ obtained by passing a running annual mean across the same monthly fluxes; (c) the same deseasonalized fluxes with their long-term mean subtracted, giving the interannual variability (IAV) \mathbf{x}^{IAV} ; and (d) the 13-model mean IAV, bounded by the 1 σ intermodel spread (dark gray), the 13-model RMS 1 σ estimation uncertainty (light gray), and the RSS of the two (outer envelope).

Latitudinal Grouping		Original 22 Regions	Continent-/Basin-Scale Grouping
Northern Total	Northern Land	Boreal N America Temp. N America	North America
		Boreal Asia Temperate Asia Europe	Eurasia
	Northern Oceans	Northern Ocean North Atlantic	Atlantic 15°N+
		North Pacific	N. Pacific
Tropical Total	Tropical Oceans	West Pacific East Pacific	Tropical Pacific
		Tropical Atlantic Tropical Indian	
	Tropical Land	Northern Africa Tropical America	
		Tropical Asia	Australasia
Southern Total	Southern Land	Australia	
		Southern Africa Temp. S America	
	Southern Oceans	South Atlantic South Pacific South Indian Southern Ocean	

Figure 3. Grouping of the 22 regions used to get the latitudinal results and the continent-/basin-scale results.

where \mathbf{E} is a matrix that applies the long-term means to each of the N months in \mathbf{x}^{IAV} . We briefly compare our \mathbf{x}^{mean} results here to the earlier TransCom results of G03 and G04, but we devote most of our attention to the IAV results given in \mathbf{x}^{IAV} . We will present our seasonal cycle results $\mathbf{x}_i^{\text{seas}}$ elsewhere: they are similar to the seasonal results of G04.

[22] Equation (3) gives an a posteriori error covariance matrix \mathbf{P}^{mon} that reflects the uncertainty in the estimated monthly flux magnitudes \mathbf{x}^{mon} . Corresponding covariance matrices for the deseasonalized fluxes $\mathbf{x}^{\text{deseas}}$, the seasonal fluxes \mathbf{x}^{seas} , the interannual variability \mathbf{x}^{IAV} , and the long-term mean fluxes \mathbf{x}^{mean} may be calculated as

$$\begin{aligned}
 \mathbf{P}^{\text{deseas}} &= [\mathbf{D}]\mathbf{P}^{\text{mon}}[\mathbf{D}]^T, \\
 \mathbf{P}^{\text{seas}} &= [\mathbf{I} - \mathbf{D}]\mathbf{P}^{\text{mon}}[\mathbf{I} - \mathbf{D}]^T, \\
 \mathbf{P}^{\text{mean}} &= [\mathbf{M}]\mathbf{P}^{\text{deseas}}[\mathbf{M}]^T, \\
 \mathbf{P}^{\text{IAV}} &= [\mathbf{I} - \mathbf{EM}]\mathbf{P}^{\text{deseas}}[\mathbf{I} - \mathbf{EM}]^T,
 \end{aligned} \tag{7}$$

where \mathbf{D} and \mathbf{M} are matrices embodying the running and long-term means in equations (4) and (5), such that

$$\begin{aligned}
 \mathbf{x}^{\text{deseas}} &= \mathbf{D}\mathbf{x}^{\text{mon}} \\
 \mathbf{x}^{\text{mean}} &= \mathbf{M}\mathbf{x}^{\text{deseas}}.
 \end{aligned} \tag{8}$$

The uncertainties σ^{deseas} and σ^{IAV} given by $\mathbf{P}^{\text{deseas}}$ and \mathbf{P}^{IAV} may be thought of as those in the estimated annual mean for any given year in the span, while those given by \mathbf{P}^{mean} are

for the over-all long-term mean (for 1988–2003, $\sim \sqrt{16}$ times smaller).

[23] In section 3, we present the results for the 22 estimated regions grouped into larger regions as shown in Figure 3. If this grouping is represented with transformation matrix \mathbf{T} such that $\mathbf{x}_{\text{grouped}} = \mathbf{T}\mathbf{x}$, then the covariances for the larger regions are found as $\mathbf{P}_{\text{grouped}} = \mathbf{T}\mathbf{P}\mathbf{T}^T$.

[24] In contrast to the estimated uncertainties discussed above, which quantify random errors in the estimated fluxes due to random errors in the measurement/model mismatch, we may also calculate uncertainties in the estimate caused by errors in the transport models. To do this we assume that the 1σ standard difference obtained in the estimated fluxes across the 13-member sample of transport models is a useful estimate of the difference between any one of these models' estimates and the true fluxes. We may define 1σ transport uncertainties in $\mathbf{x}_i^{\text{mon}}$, \mathbf{x}^{mean} , $\mathbf{x}_i^{\text{seas}}$, $\mathbf{x}_i^{\text{deseas}}$, and $\mathbf{x}_i^{\text{IAV}}$ as

$$\left(\text{tr } \sigma_{ij}^{\text{type}}\right)^2 = \text{Var}\left(x_{ij}^{\text{type}}\right), \tag{9}$$

where type is “mon,” “mean,” “seas,” “deseas,” or “IAV,” where i and j are the time and region indexes, and where $\text{Var}()$ indicates the sample variance across the 13 transport models. Examples of both the estimation uncertainties and the transport uncertainties are given in Figure 2 d for the estimated flux IAV for Europe.

3. Results

3.1. Long-Term Mean Results

[25] Table 3 shows the 1992–1996 mean fluxes from \mathbf{x}^{mean} for each region (averaged across all 13 models) from our interannual inversion, compared with those of the TransCom 3 annual-mean (G03) and cyclo-stationary (G04) inversions for the same period. Note that these inversions all used different sets of measurements (75 sites for G03 and G04 versus a very different 78 sites here), transport models (16 in G03, 12 in G04, 13 here), measurement uncertainties, and a priori uncertainties. Despite this, the inversions give quite similar results for the 22 regions, generally agreeing to within the 1σ uncertainties given in Table 4. Two regions, the Tropical Indian Ocean and the Southern Ocean, differ by more than 2σ , both having less uptake in this study. At the coarser scales, our results agree more closely with the seasonal inversion of G04 than the annual mean inversion of G03. Partially this is due to closer agreement in the set of transport models used; however, we should also expect our interannual inversion to give results closer to an inversion that solves for the seasonal cycle (G04) than one that specifies it beforehand (G03), since specifying an incorrect seasonal cycle shape could lead to biases.

[26] On the coarsest scale, our global total flux (land + ocean) differs significantly (by 2σ) from that of both G03 and G04 due to differences in the average fossil fuel burning input and atmospheric CO₂ increase rate for 1992–1996 imposed on the inversions. In the annual mean inversion of G03 and the seasonal inversion of G04, the atmospheric increase rate must be imposed as an explicit constraint (since the interannual trend in the data is removed in computing the

Table 3. Long-Term Mean Flux Estimates From This Study Averaged Across 1991–2000 and 1992–1996, Compared With the 1992–96 Means From the TransCom 3 Annual Mean Inversion of Gurney *et al.* [2003] and Seasonal Inversion of Gurney *et al.* [2004]^a

Region	Prior	1992–1996			1991–2000
		G03	G04	IAV	IAV
Boreal N America	0.00	0.28	0.20	0.20	0.14
Temp. N America	-0.54	-0.82	-0.89	-1.26	-1.11
Tropical America	0.55	0.67	0.74	0.91	1.07
Temp. S America	0.00	-0.12	-0.24	-0.57	-0.64
Northern Africa	0.15	-0.01	0.79	0.40	0.50
Southern Africa	0.15	-0.29	-0.51	-0.58	-0.62
Boreal Asia	-0.40	-0.60	-0.36	-0.37	-0.33
Temperate Asia	0.30	-0.42	-0.41	-0.24	-0.31
Tropical Asia	0.80	0.42	0.27	0.27	0.29
Australia	0.00	-0.15	-0.10	-0.09	-0.11
Europe	-0.10	-0.61	-0.96	-1.03	-0.97
North Pacific	-0.50	-0.25	-0.32	-0.44	-0.56
West Pacific	0.15	-0.15	-0.21	-0.10	-0.11
East Pacific	0.47	0.63	0.66	0.54	0.57
South Pacific	-0.23	0.49	0.51	0.22	0.09
Northern Ocean	-0.41	-0.30	-0.27	-0.23	-0.22
North Atlantic	-0.29	-0.45	-0.29	-0.28	-0.29
Tropical Atlantic	0.13	-0.05	-0.10	0.09	0.09
South Atlantic	-0.13	-0.04	-0.05	-0.12	-0.21
Southern Ocean	-0.88	-0.47	-0.55	-0.28	-0.25
Tropical Indian	0.12	-0.34	-0.33	0.12	0.24
South Indian	-0.56	-0.24	-0.39	-0.45	-0.41
Northern land	-0.74	-2.16	-2.42	-2.69	-2.58
Tropical land	1.50	1.10	1.80	1.58	1.86
Southern land	0.15	-0.56	-0.85	-1.23	-1.37
Global land	0.91	-1.62	-1.46	-2.34	-2.09
Northern Oceans	-1.20	-1.00	-0.88	-0.95	-1.06
Tropical Oceans	0.87	0.09	0.03	0.65	0.78
Southern Oceans	-1.80	-0.26	-0.49	-0.65	-0.78
Global Oceans	-2.13	-1.18	-1.34	-0.95	-1.06
Northern total	-1.94	-3.16	-3.30	-3.64	-3.64
Tropical total	2.37	1.19	1.83	2.24	2.64
Southern total	-1.65	-0.82	-1.34	-1.88	-2.14
Global total	-1.22	-2.80	-2.81	-3.29	-3.15

^aIAV, this study; G03, Gurney *et al.* [2003]; G04, Gurney *et al.* [2004]. Units are PgC yr⁻¹. The annual mean a priori fluxes (Prior) assumed in all three studies are also given.

average data for the inversion), while here this constraint is implicit in the interannual trend contained in the data. The global atmospheric increase rate implied by our weighted CO₂ time series is 0.30 PgC yr⁻¹ smaller than that used in G03/G04 (2.97 versus 3.274 PgC yr⁻¹). Taken together with a higher fossil fuel input rate (6.26 versus 6.10 PgC yr⁻¹), this implies a global total uptake 0.46 PgC yr⁻¹ stronger than in G03/G04. This appears in our inversion as 0.88 PgC yr⁻¹ more uptake in the extratropics compared to the seasonal inversion of G04 (with the north/south difference changing little), counterbalanced by 0.41 PgC yr⁻¹ more outgassing in the tropics. In terms of the land/ocean breakdown, we find 0.88 PgC yr⁻¹ more uptake by the land biosphere than G04 (spread broadly across all latitudes), compensated by 0.39 PgC yr⁻¹ less uptake by the oceans, mostly due to a 0.62 PgC yr⁻¹ greater outgassing in the tropical oceans. Though our ocean fluxes in both the tropics and extratropics are closer to the Takahashi *et al.* [1999] estimates than the G04 results are, the higher outflux in the tropics

Table 4. Transport and Estimation Errors in \mathbf{x}_{IAV} Computed for Each Region, Plus the Significance of the estimated interannual Variability^a

	Prior Error	Post. Error	Model Error	χ^2_0	$N_{ind}/(1+s^2)$		
					0.20	1.00	2.00
Boreal N. America	0.35	0.19	0.14	4.0	1.00	0.97	0.72
Temp. N. America	0.84	0.23	0.22	22.7	0.52	0.02	0.00
Tropical America	1.34	0.69	0.41	2.3	1.00	1.00	0.95
Temp. S. America	0.87	0.51	0.27	11.7	0.92	0.39	0.02
Northern Africa	0.77	0.50	0.28	13.1	0.88	0.29	0.01
Southern Africa	0.93	0.48	0.31	1.1	1.00	1.00	1.00
Boreal Asia	0.70	0.24	0.18	4.3	1.00	0.96	0.66
Temperate Asia	0.79	0.25	0.24	8.4	0.98	0.68	0.12
Tropical Asia	0.60	0.31	0.25	36.0	0.14	0.00	0.00
Australia	0.32	0.12	0.09	16.9	0.75	0.11	0.00
Europe	0.70	0.19	0.14	55.7	0.01	0.00	0.00
North Pacific	0.28	0.14	0.09	69.9	0.00	0.00	0.00
West Pacific	0.20	0.13	0.09	2.8	1.00	0.99	0.90
East Pacific	0.22	0.14	0.05	61.8	0.00	0.00	0.00
South Pacific	0.38	0.20	0.14	30.6	0.25	0.00	0.00
Northern Ocean	0.16	0.09	0.04	30.4	0.26	0.00	0.00
North Atlantic	0.18	0.13	0.06	3.5	1.00	0.98	0.81
Tropical Atlantic	0.18	0.14	0.05	5.2	1.00	0.92	0.49
South Atlantic	0.20	0.15	0.06	17.0	0.75	0.11	0.00
Southern Ocean	0.46	0.11	0.06	22.3	0.53	0.02	0.00
Tropical Indian	0.26	0.18	0.08	25.2	0.42	0.01	0.00
South Indian	0.21	0.12	0.06	2.9	1.00	0.99	0.89
North America	0.91	0.25	0.24	23.2	0.50	0.02	0.00
Eurasia	1.26	0.28	0.25	20.0	0.63	0.05	0.00
North Pacific	0.28	0.14	0.09	69.9	0.00	0.00	0.00
Atlantic 15°N+	0.24	0.16	0.08	2.0	1.00	1.00	0.97
Africa	1.21	0.61	0.41	12.6	0.90	0.32	0.01
South America	1.60	0.66	0.43	2.9	1.00	0.99	0.89
Australasia	0.68	0.33	0.27	54.0	0.01	0.00	0.00
Tropical Pacific	0.30	0.18	0.11	23.0	0.51	0.02	0.00
Northern land	1.55	0.28	0.23	103.	0.00	0.00	0.00
Tropical land	1.66	0.69	0.46	56.8	0.01	0.00	0.00
Southern land	1.31	0.56	0.31	21.1	0.58	0.03	0.00
Global land	2.62	0.53	0.29	574.	0.00	0.00	0.00
Northern oceans	0.37	0.22	0.13	31.6	0.23	0.00	0.00
Tropical oceans	0.44	0.30	0.14	21.5	0.57	0.03	0.00
Southern oceans	0.66	0.27	0.19	19.5	0.65	0.05	0.00
Global ocean	0.88	0.47	0.27	36.4	0.13	0.00	0.00
Northern total	1.59	0.22	0.22	59.7	0.01	0.00	0.00
Tropical total	1.72	0.58	0.44	83.7	0.00	0.00	0.00
Southern total	1.47	0.45	0.30	25.8	0.40	0.01	0.00
Global total	2.76	0.25	0.13	6228.	0.00	0.00	0.00

^aOn the left, the a priori and a posteriori flux estimation uncertainties (1σ) in \mathbf{x}_{IAV} are given for each region, along with the sample standard deviation across the 13 models' monthly \mathbf{x}_{IAV} estimates, taken as a proxy for the transport model error (all three in units PgC yr⁻¹). The a posteriori and model errors are RMS values across 1991–2000. On the right, the significance of the estimated IAV for each region is given as the probability that the null hypothesis is correct according to the χ^2 test ($\nu = 11$). The null hypothesis is that the estimated IAV in \mathbf{x}_{IAV} is consistent with that of a time series with zero underlying IAV but with random errors having a 1σ uncertainty equal to the RSS of the model-dependent (“transport”) uncertainties and the estimation uncertainties. Low probabilities suggest that a true underlying flux variability may be discerned robustly above the “noise” of the estimation and transport errors. Prior is a priori, Post. is a posteriori, N_{ind} is the number of independent models in the 13-model sample, s is the target signal-to-noise ratio tested for, and χ^2_0 is the computed single-model value ($N_{ind} = 1$) using $s = 0$.

pushes our total ocean uptake to under 1 PgC yr⁻¹; most of the difference from the Takahashi et al. global totals is due to a reduction of over 1 PgC yr⁻¹ in the uptake of the extra-tropical southern oceans.

[27] Table 3 also gives our mean flux results for 1991–2000, a period that includes the global CO₂ release associated with the 1997/1998 El Niño. The fluxes for this period differ only slightly from the 1992–1996 interannual inversion results, far less than the 1992–1996 interannual inversion results differ from the 1992–1996 results of G03 and G04, suggesting that the impact of the El Niño may be smaller than the procedural differences between the inversions. Comparing our 1992–1996 results with the latitudinal totals for 1990–1996 from Figure 3.5 of *Prentice et al.* [2001], we obtain greater tropical CO₂ release and greater extratropical uptake than the inversions compiled there. Much of this difference is due to their broader definition of the tropics ($\pm 30^\circ$) and the fact that most of our Southern Land region lies north of 30°S. Our finding of nearly 3 times more land than ocean uptake in the extratropical north is clearly quite different from their compiled results, though.

3.2. Interannual Variability Results

[28] The full time-dependent flux inversion outlined in section 2 generates a sizable volume of output: 192 monthly flux values and their accompanying estimation uncertainties and correlations for 22 regions, for each of 13 different transport models. We use model-mean time series plots like that presented in Figure 2d to summarize our \mathbf{x}^{IAV} results here, starting with the coarsest spatial scales first, then moving to the finer scales. As in Figure 2d, the 1 σ intermodel spread (our proxy for transport uncertainty) is given by the dark error bands, while the 1 σ estimation uncertainty from \mathbf{P}^{IAV} (which is generally greater) is given by the lighter bands; the root-mean square (RMS) values for these across 1991–2000 are given in Table 4. The root-sum-square (RSS) of these two uncertainties, given as the outer band, is used to assess the robustness of the estimated flux IAV. As we examine the results at progressively finer scales, we are interested in finding when these RSS uncertainties become large enough to render the IAV results statistically insignificant. For those regions with significant IAV, we discuss what physical mechanisms might be driving it. We discuss only the 13-model mean flux results here; the issue of which individual models do the best job in explaining the measurements will be left to a subsequent study.

3.2.1. The χ^2 Significance Test for the Interannual Variability

[29] The 1 σ transport and estimation uncertainties given in Figure 2d (and in upcoming Figure 4–8) characterize those we would expect for any one model in our set of 13. Because of cancellation of errors, we would expect the corresponding uncertainties in the 13-model mean to be smaller; a χ^2 test is used here to test the significance of these 13-model mean IAV results. The mathematical description of this test, its statistical meaning, and how it may also be used to test the significance of any one model's results, are given in Appendix B. A flux time series' IAV is considered “significant” here if the test probability $P \leq 0.01$, “marginally significant” for $P = 0.01–0.05$, and “not

significant” for $P \geq 0.05$. Test probabilities P for each 13-model mean flux IAV time series are given in the $N_{\text{ind}}/(1 + s^2) = 1.00$ column of Table 4; these will be used in the discussion of the results below.

[30] In our significance test, we have not considered the additional source of uncertainty due to the choice of measurement sites used in the inversion. *Gurney* [2004] assesses this uncertainty for TransCom 3 interannual inversions similar to those presented here, and *Baker* [2001] and *Rödenbeck et al.* [2003] have done so in the single-model framework. The issue of station selection seems to impact the seasonal and long-term mean results more than the IAV, and is less important when larger numbers of sites are used, as is the case here.

3.2.2. Total (Land + Ocean) Flux: Globally and by Latitude

[31] The global total (land + ocean) flux is the most well-constrained term in the problem, because it is set broadly by the difference between the slowly varying anthropogenic fossil fuel input and the well-measured accumulation rate of CO₂ in the atmosphere. The estimated total flux IAV (Figure 4a) has a monthly estimation uncertainty of ~ 0.25 PgC yr⁻¹, with an intermodel spread of only ~ 0.13 PgC yr⁻¹. The high uncertainty in the deforestation and biomass burning input terms do not contribute to this error, as these terms are lumped together with the natural land biospheric source.

[32] Figures 4b–4d give the total flux (land + ocean) for three broad latitude bands defined in Figure 3; both the estimation uncertainties and the intermodel spread have increased substantially over the global values. The estimation uncertainties (Table 4) are low (~ 0.22 PgC yr⁻¹) in the extratropical north, higher (~ 0.45 PgC yr⁻¹) in the extratropical south, and highest (~ 0.58 PgC yr⁻¹) in the tropics. Intermodel differences (Table 4) are generally $\sim 30\%$ lower than the estimation uncertainties in the tropics and south, and are about as strong as them in the north.

[33] Both the estimation and transport uncertainties are low enough to permit the main features of the flux variability for these latitudinal totals to be estimated. The global, northern, and tropical total IAVs were highly significant ($P < 0.0001$), while the southern total was marginally significant at $P = 0.01$ (Table 4). The outgassing spike seen globally at the time of the 1997/1998 El Niño is allocated mainly to the tropics, as is the global uptake following the Mount Pinatubo eruption in mid-1991.

3.2.3. Land/Ocean Flux Partition: Globally and by Latitude

[34] Figures 5b–5d give the flux results for the same three broad latitude bands, partitioned into land and ocean components as in Figure 3. The a posteriori estimation uncertainties (Table 4) for the ocean bands in the tropics/south are less than half those of the land bands in the tropics/south. While part of this is due to the tighter a priori uncertainties assumed over the ocean regions, most of it is due to the stronger measurement constraint there (almost all the sites measure marine air in those latitudes). The estimation uncertainties for both land and ocean in the north are low because of the greater measurement density there than in the tropics/south. The highest estimation

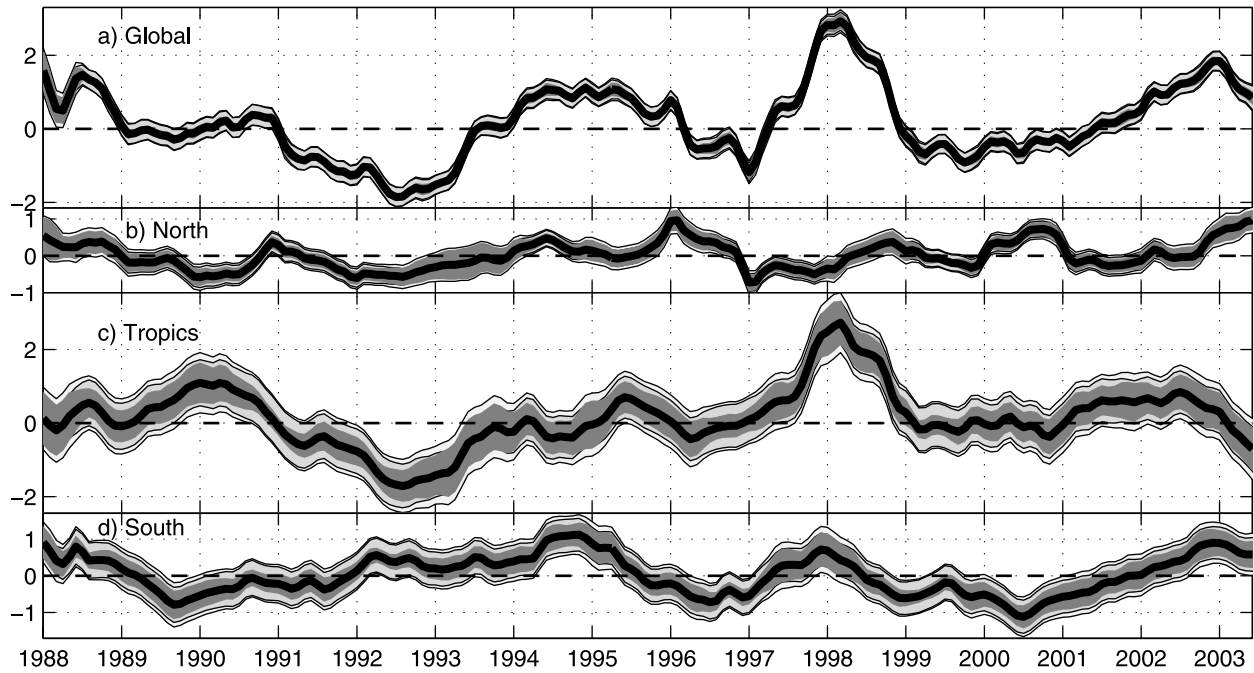


Figure 4. Total flux (land + ocean) interannual variability (PgC yr^{-1}) from \mathbf{x}^{IAV} for the full globe, and for the three latitude bands defined in Figure 3. The 13-model mean (black line) is bounded by the 1σ inter-model spread (dark shading), the 13-model RMS 1σ estimation uncertainty (light shading), and the RSS of the two (outer envelope).

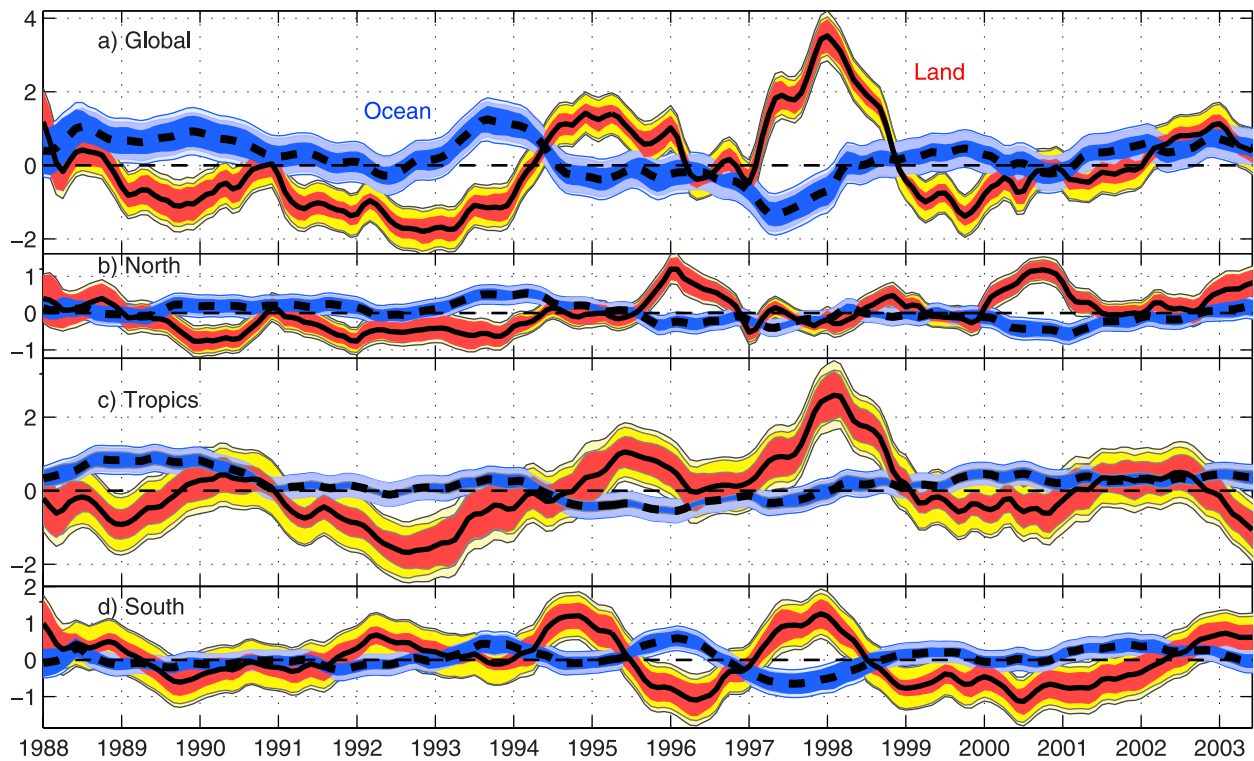


Figure 5. Flux interannual variability (PgC yr^{-1}) from \mathbf{x}^{IAV} for the full globe, and for the three broad latitude bands defined in Figure 3, partitioned into land fluxes (solid lines) and ocean fluxes (dashed lines).

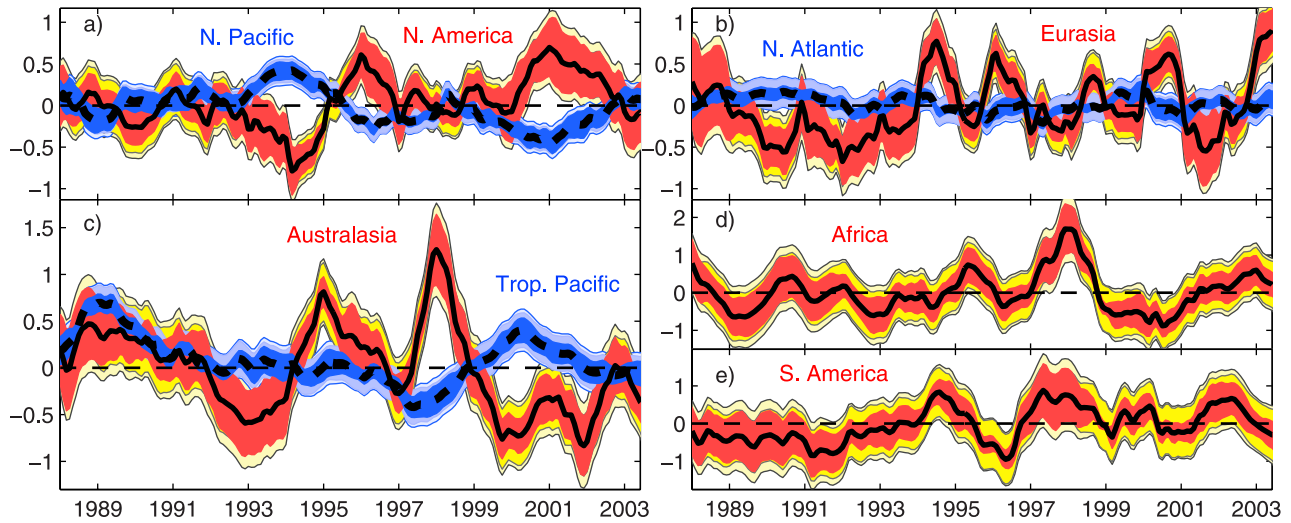


Figure 6. The 13-model mean CO₂ flux IAV (PgC yr⁻¹) from x^{IAV} for several continents (solid lines) and ocean basins (dashed lines) defined in Figure 3: (a) North Pacific and North America, (b) Atlantic north of 15°N and Eurasia, (c) Australasia and Tropical Pacific, (d) Africa, and (e) South America (note the different scales for Africa and South America).

uncertainties are obtained for the tropical/southern land regions; this is due not only to the lack of measurement sites over these regions, but also to the prevalence of convective motions there which transport the effect of the fluxes away from the measurement sites, most of which are at the surface.

[35] The 1 σ inter-model spreads are 30% to 50% lower than the estimation uncertainties in this six-region partition, except for the Northern Land region where they are more closely equal. For that region, the estimation uncertainties are kept low by the high measurement density, while the intermodel spread is kept high by the strongly varying land

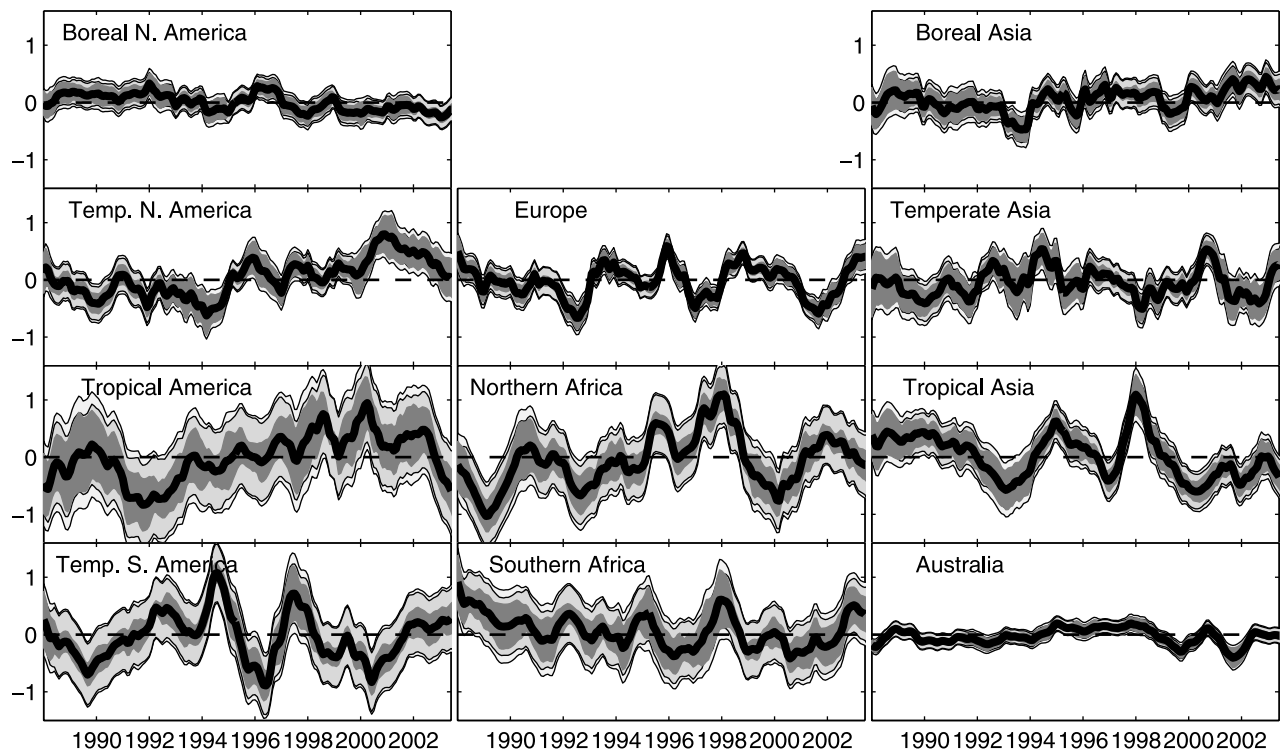


Figure 7. The 13-model mean CO₂ flux IAV (PgC yr⁻¹) from x^{IAV} for the 11 land regions shown in Figure 1.

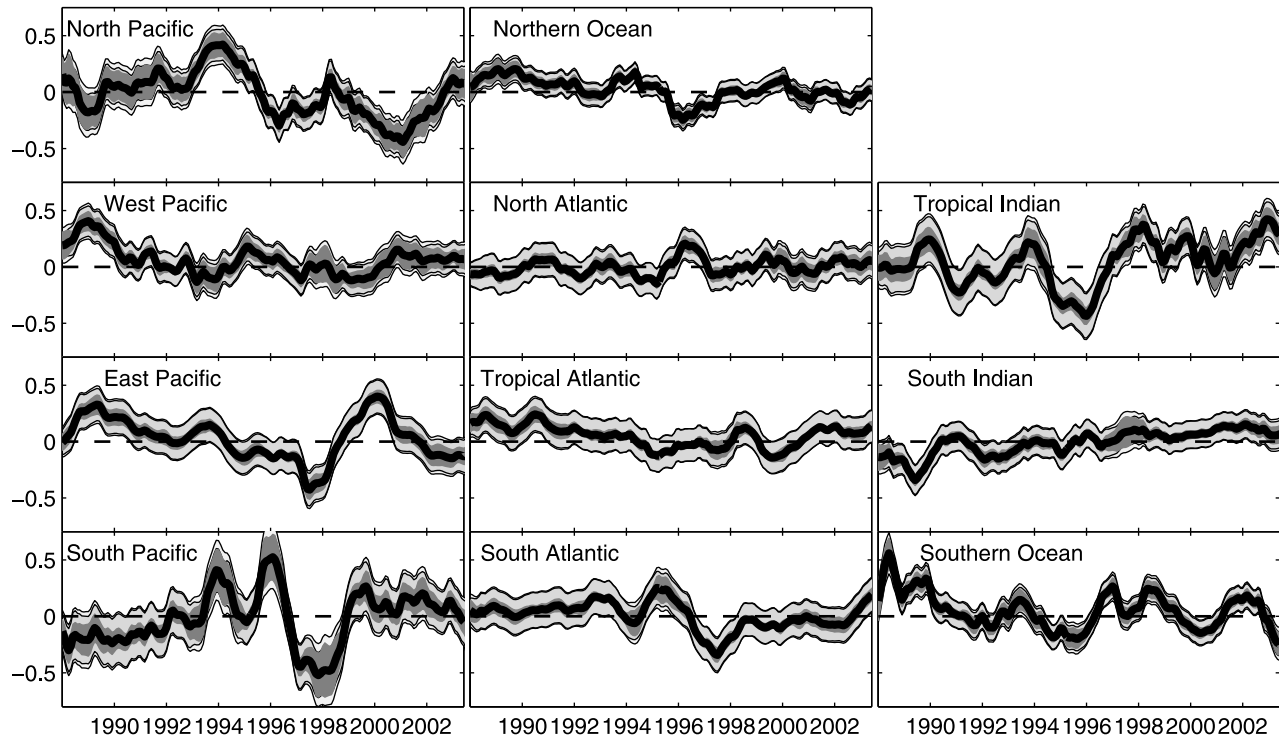


Figure 8. The 13-model mean CO₂ flux IAV (PgC yr⁻¹) from x^{IAV} for the 11 ocean regions shown in Figure 1. Note that the scale here is twice as fine as in Figure 7.

biosphere there interacting with seasonal differences in mixing out of the boundary layer between the models.

[36] The transport and estimation uncertainties are low enough that the land and ocean flux IAV may be separated robustly for most of these latitude bands (Table 4). The IAV for all six regions is significant at $P < 0.01$ except for the Tropical Oceans (marginally significant at $P = 0.03$) and the Southern Land/Ocean partition (marginally significant at $P = 0.03/0.05$).

[37] The IAV for the Northern Land is the most robust of those for the six regions in this partition, not because it has the largest variability, but rather because its combined estimation and transport uncertainties are low. The IAV for the Tropical Land is robust, however, not because its transport and estimation uncertainties are any lower (they are substantially higher) but because the variability found there is so much greater. The inversion locates the outgassing at the time of the 1997/1998 El Niño squarely in the tropical land regions, and puts the post-Pinatubo uptake in 1992 there as well. If the flux for South Africa was grouped with the tropics (instead of in the south as it is here, following the convention of G03 and G04) the 1997/1998 El Niño outgassing event would be an extra 0.5 PgC yr⁻¹ stronger. The IAV in the oceans, while significant, is not as strong as the land variability. The tropical ocean variability shows a moderate uptake immediately preceding the 1997/1998 El Niño, and moderate carbon release after (with marginal significance, $P = 0.02$). The southern land/ocean regions (with marginal significance) show counter-balancing carbon release/uptake events during the early part of the 1997/1998 El Niño, preceding the tropical land release event.

[38] When the land and ocean totals for the three latitude bands are summed to give a global land/ocean partition (Figure 5a), the resulting variability is highly significant ($P < 0.0001$). The most notable feature is again the 1997/1998 El Niño outgassing event attributed to the land, preceded by a prominent ocean uptake in 1997. The overall land IAV is about twice as strong as the ocean IAV, but this is largely set by the relative tightness of the land/ocean a priori uncertainties. When the a priori constraint on the ocean regions is set as loosely as that for the land regions, the global land/ocean partition is more equally divided; the ocean IAV patterns remain similar, but their amplitudes increase.

3.2.4. Continent- and Basin-Scale IAV Results

[39] Before examining the IAV for the 22 regions, we consider the fluxes on the continent and basin scale: in the north, for Eurasia, North America, the Atlantic north of 15°N, and North Pacific; in the tropics for the full Tropical Pacific, Australasia, Africa, and South America (Figure 6). For the four northern regions, the estimation uncertainties and especially the transport uncertainties are large enough that the longitudinal partition is of only marginal significance (Table 4). The North Pacific variability is highly robust ($P < 0.0001$), but the Eurasian and North American variabilities are significant at only $P = 0.05$ and 0.02, respectively. The variability for the Atlantic north of 15°N is not significant, not because the uncertainties are high there, but because the inversion found little variability. The estimation uncertainties on these scales are small enough that the transport uncertainty is often the larger of the two error terms. The flux IAV for the North Pacific is dominated

by a reduction in CO₂ uptake in 1993–1994, trending to an increased uptake in 2000–2001.

[40] In the tropics/south, the variability for Australasia was highly significant, while that for South America and Africa not at all; if South America and Africa are combined into a single region, however, that variability is also highly significant. The variability in the full Tropical Pacific (East+West) is marginally significant at $P = 0.02$.

3.2.5. IAV Results for the Original 22 Regions

[41] The flux estimates for the original 22 regions are given in Figures 7 and 8. For the most part, the estimation and transport uncertainties (Table 4) are larger for the land than the ocean regions. Because of this the land region results are generally less significant than the ocean region results, even though the IAV for the land regions tends to be greater. The largest IAV is found in the tropical land regions and Temperate South America, with secondary IAV in the temperate northern land regions, the South, East, and North Pacific, the Tropical Indian Ocean, Boreal Asia, and South Africa. When significance is considered, however, the most robust IAV on land is found in Tropical Asia and Europe ($P < 0.01$) with that in Temperate North America ($P = 0.02$) of marginal significance (Table 4). The variability for the other land regions (most notably in Africa and South America) is not significant, although Australia ($P = 0.11$) is close.

[42] Significant IAV ($P < 0.01$) is found for the East, North, and South Pacific regions, and the Northern Ocean, while the IAV for the Tropical Indian and Southern Oceans is marginally significant. The variability for the remaining ocean regions is quite low and not significant. Note that the scale on the y-axis of the ocean plots in Figure 8 has been expanded to twice that of the land plots.

4. Discussion

4.1. Key IAV Results and Possible Physical Driving Mechanisms

[43] Our inversion attributes the main features of the global CO₂ flux variability for 1988–2003, especially the release of CO₂ in 1997/1998 and the relative uptake of late 1991 to early 1993, to the tropics (Figure 4) and to the tropical land regions in particular, both with high significance. The variability in the extratropical north is 2 to 3 times less, though of even higher significance given the lower uncertainty there (Figure 5). The partition of the variability into latitudinal land and ocean totals is statistically robust, although marginally so for the tropical oceans and extratropical south. When the latitude bands are partitioned into individual continents and basins, the significance of the variability becomes marginal in the north, and is lost altogether in the tropics, except for the well-observed Tropical Pacific and Australasia. On the scale of the 22 individual regions (Figures 7 and 8), Tropical Asia, Europe, and (marginally) Temperate North America are robust on land, while for the oceans, the North, East, and South Pacific, the Northern Ocean, and (marginally) the Southern Ocean and Tropical Indian are significant.

[44] For these regions that we believe have significant variability (i.e., reflecting a real underlying flux signal, with a signal-to-noise ratio $s \geq 2$ here), we may consider what

physical or biological processes may be driving it. Our results for the East Pacific have a clear physical driver: the increased uptake before and during the 1997/1998 El Niño warm phase is consistent with the capping of the tropical thermocline then, which reduces the usual outgassing of CO₂-rich waters. The increased CO₂ release later agrees with the opposite condition, the increased shoaling of the thermocline there during the strong La Niña of 1999–2000. The 0.4 PgC yr⁻¹ reduction in East Pacific outflux we obtain in 1997 compared to non-El Niño conditions agrees well with a similar reduction of about 0.4 PgC yr⁻¹ estimated from Table 2 of *Feely et al.* [2002] for that year based on in situ measurements scaled up to the broader equatorial Pacific. Our strong uptake during 1997/1998 in the South Pacific suggests that this ENSO-driven effect may act south of 15°S, as well.

[45] The highly significant variability in Tropical Asia is also physically interpretable: the timing and magnitude of the release of CO₂ centered on early 1998 agrees well with the large Indonesian fires observed at that time, driven by ENSO-induced drought conditions (*Page et al.* [2002] estimate a release of 0.81–2.57 PgC from the Indonesian fires between June 1997 and March 1998). The relative uptake of carbon there in 1992–1993 could be due to effects of the June 1991 Pinatubo eruption, though the net fluxes estimated in this analysis do not by themselves allow us to distinguish between the possible causes (decreased autotrophic or heterotrophic respiration, increased photosynthesis, decreased incidence of fires).

[46] Patterns of variability of equally high significance are found, however, for some regions (the North and South Pacific, and the Northern Ocean) for which there are no obvious driving processes. For weakly constrained regions with high variability like the South Pacific, having all the constraining measurement sites on one corner of the region may cause a sensitivity to the data that is not fully reflected in the a posteriori uncertainties. This may be the case for the Tropical Indian Ocean, as well: It is constrained largely by a single station at Seychelles. As noted in Appendix A, we have added an extra 1.0 ppm measurement uncertainty to the Seychelles site for 1988–1996 to account for measurement problems then. This value may still be too low: If this extra uncertainty is increased to 1.5 ppm across the same span, the variability for the Tropical Indian is reduced by a factor of 2 beyond what is shown in Figure 8. Further sensitivity studies are required to investigate such regions that return significant variability with our current uncertainty estimates, but for which no clear physical drivers have been found.

[47] The largest IAV estimated in our inversions outside of Tropical Asia, that for the four regions in South America and Africa, is not significant on the scale of the original regions, or when they are grouped into two continents: the estimation uncertainty for these regions is too high, because of the sparsity of measurement sites near them. If grouped into a single Africa/South America region, however, the variability is highly significant. If we understand that the sparsity of data in the tropics primarily impacts these two regions, then there is no need to disregard our tropical results altogether: We may discuss robust variability of the

well-observed Tropical Asia, Australia, and East Pacific regions separately, and discuss the rest of the tropics grouped together as necessary to obtain significant results. With this approach, South America and Africa together account for almost as much uptake as Tropical Asia post-Pinatubo, and at least as much outgassing during the 1997/1998 El Niño.

4.2. Comparison to Previous Studies

[48] As the uncertainties in the 13-model mean IAV estimates discussed above are assumed here to be $\sqrt{5}$ times lower than those in the IAV obtained using any one of the models (assuming $N_{\text{ind}} = 5$; see Appendix B for details), the significance of the single-model IAVs is even less than those discussed above. Using the $N_{\text{ind}}/(1 + s^2) = 0.2$ column of Table 4 to test these single-model significances (as described in Appendix B), we find that only 3 of the 22 emission regions have robust IAV: the North and East Pacific, and (marginally) Europe. On the coarser scales, only the northern and tropical land IAVs, the northern and tropical total (land+ocean) IAVs, and (marginally) the global land/ocean partition are significant. Since previously published CO₂ flux IAV studies have generally used measurement and a priori constraints of approximately equal or looser magnitude than those used here, one might expect our low single-model significances to apply to their results, too. To a large extent, this may explain why there has been so little agreement between the results obtained from the different studies.

[49] *Bousquet et al.* [2000] (B00) have attributed the anomalous post-Pinatubo global uptake to the northern extratropical land regions, especially North America. We do find a sharp uptake spike in the combined North America region (boreal+temperate) of 0.5 PgC yr⁻¹ here, but it is in 1994, too long after the June 1991 eruption to be directly related to it. Our uptake for Temperate North America is roughly 0.6 PgC yr⁻¹ greater before 1995 than after, but is roughly constant across 1989–1995; no clear post-Pinatubo signal is seen. In our results, the feature in the north most likely to be related to the Pinatubo eruption is the 0.5 PgC yr⁻¹ uptake event in Europe in 1992. Part of the explanation for the strong post-Pinatubo North American CO₂ sink found in B00 may be due to the TM2 model they used. In our study here, the North American x^{IAV} for the TM2 model was offset -0.4 PgC yr⁻¹ across 1992–1994 compared to the 13-model mean. Our global land flux total looks broadly similar to theirs, but our global ocean total is quite different: B00 have a negative ocean excursion in 1995–1996 and a positive excursion in 1997/1998, while we have a large negative excursion in 1997 during the early edge of the El Niño. Our Tropical Pacific results also look broadly similar, with outgassing in 1989 trending toward uptake by 1997, but our tropical land totals show little resemblance to theirs: differences in station selection (we use the Tokyo-Sydney flight data, they use the South China Sea ship tracks) and the temporal coverage of the measurement time series may be especially important for this underconstrained area.

[50] Additional details on the B00 results have been given by *Peylin et al.* [2005], including land and ocean totals for

three broad latitude bands. In general, there is little agreement between our latitudinal land/ocean IAV results and theirs; this may be partially due to the somewhat tighter a priori uncertainties they apply to South America and Africa, which may drive some of the IAV out of the tropics into the north. Their results for the North Atlantic agree broadly with ours, however, including uptake there in 1995.

[51] The most thorough study of regional CO₂ flux estimates for the full globe published to date is that of *Rödenbeck et al.* [2003]. They used fewer measurement times series than we do (from 16 to 35 CMDL sites in overlapping fixed networks across 1986–2000) and solved for more regions (~ 800 , at the $\sim 8^\circ \times 10^\circ$ resolution of the model); thus more of an explicit a priori constraint was required (i.e., in terms of explicit correlations between neighboring regions in the a priori covariance matrix, rather than implicitly in the shape of the prespecified fluxes inside each region, as is done here). They used a priori uncertainties proportional to net primary production (NPP) over land, and flat uncertainty fields over the ocean, with interregion correlations given by exponential decay with e-folding lengths of 1275 km over land and 1912 km over the ocean. This choice of a priori constraint allowed the largest deviations from the prior where the local NPP was largest: over the tropical land regions, and over Amazonia in particular. Their strongest flux IAV was in fact obtained in the tropical land regions, especially South America, with less in the northern land and relatively little in the oceans (especially after 1996 when they used the most sites). Our global land IAV agrees well with theirs, though our ocean IAVs differ more. We obtain ocean uptake in 1997, for example, that they do not get. Interestingly, we both obtain a 1 PgC yr⁻¹ ocean outgassing event in 1993–1994, though ours occurs a few months earlier.

[52] At the continent/basin scale, the only areas for which we clearly agree with *Rödenbeck et al.* [2003] are in North America and Tropical Asia/Australia, both from the mid-1990s on. We find the same timing of outgassing around the 1997/1998 El Niño from Tropical Asia, but have a somewhat larger response; they place more of the tropical response at that time in South America than we do, perhaps due to the different constraint approach and the fewer number of tropical measurements used. On the scale of our original 22 regions, we show fair agreement for the IAV of Temperate North America going all the way back to 1991, and good agreement in Tropical Asia and Europe back to 1996. Interestingly, these are also the only land regions for which we feel our IAVs are significant. It is perhaps also significant that the agreement in Tropical Asia and Europe drops off before 1996, when *Rödenbeck et al.* go from using 35 to 26 sites. For the ocean regions, we have very good agreement for the Tropical Indian ocean across the full span, but little similarity elsewhere, because of the very low IAV they obtain. In particular, there is almost no similarity in the East Pacific, a region where we feel we are obtaining physically meaningful results. Given that the a posteriori uncertainty estimates presented by *Rödenbeck et al.* are generally higher than ours for similarly sized regions, we suspect that the IAVs for at most only a few of their regions would be considered significant according to the χ^2

test performed here, even if lower transport uncertainties more appropriate for a model driven by more accurate analyzed winds were considered. Thus the disagreement between most of our estimates is actually in agreement with the low measures of significance given by our χ^2 test. The agreement that we do have occurs only for those regions with significant IAV according to the χ^2 test.

[53] Our finding that the tropical/southern land biosphere is driving the largest features in the global flux IAV is supported by the latitudinal CO₂-¹³C inversions of Piper *et al.* [2001a, 2001b] and John Miller (personal communication, 2004), which attribute the global CO₂ release of 1997/1998 to the tropical land biosphere, as well as obtaining a secondary release peak in 1995 from the same region. These inversions do not seek to separate the land and ocean areas by geographical region, but rather in terms of land and ocean flux totals inside each latitude band using ¹³C. Despite this agreement, our inversion emphasizes the difficulty of separating the land and ocean by region inside a given latitude band using the CO₂ data alone.

5. Conclusion

[54] Using identical measurements and inversion setup, we have solved for sources and sinks of CO₂ for 1988–2003 using 13 different transport model/annual wind combinations. The range in results across the models gives us a measure of the error in the CO₂ fluxes due to the transport errors in any one of the models. We use this transport uncertainty here, in combination with the estimation uncertainty, to test how much of the estimated flux IAV for each region is likely due to the error “noise” versus any actual underlying flux “signal.”

[55] No attempt has been made to match the winds used in the models to the actual winds for each year in the span; the transport errors estimated here should therefore be larger than what would be obtained in inversions using models driven by analyzed meteorological fields. Our transport errors also do not quantify any systematic errors affecting all of the models in our sample. If the north/south gradient in our forward modeled concentration field c_{fwd} averaged across all 13 of our transport models is too steep, for example, then the 13-model mean uptake we obtain in the north will be too strong, and the uptake of the southern oceans too weak, compared to the real world. This bias in our 13-model mean results will not be quantified by our transport errors, though differences due to the spread in the north/south gradient across the models will be.

[56] The uncertainty introduced into the inverted fluxes by the transport error (inferred from the 1σ between-model spread) is found here to be less than that due to the random estimation errors in the problem (Table 4), by 30–65% for the ocean regions, 20–45% for the tropical/southern land regions, and by 0–25% for the northern land regions. This extra transport uncertainty has the largest practical consequence on the IAV results in the north, where a regional partition of the variability (Figure 6) that would be statistically significant if only the estimation uncertainties were considered is rendered only marginally significant when

transport uncertainties are included. If this transport error could be reduced (for example, by using a good transport model driven by analyzed winds and vertical mixing parameters) then the possibility of partitioning the flux in the north robustly between continents and ocean basins would be re-introduced.

[57] For the tropical land regions, the random estimation error in the problem remains the dominant error source: Even if a perfect transport model were used, the utility of the results would be limited by the random errors and only the introduction of more measurements there would improve the situation. For the oceans, the transport uncertainty is generally less significant: usually only about half the estimation uncertainty. The model-dependent differences are greater over the land than the oceans, not only because mixing out of the PBL is greater there, but because the seasonal and synoptic variability of the underlying fluxes is much larger and more difficult to model, as well.

[58] Our results suggest that an inversion done using a single typical transport model driven by climatological winds would obtain significant IAV estimates for only a few of our 22 emission regions (Europe and Tropical Asia on land, the North and East Pacific for the oceans) while for the other regions the IAV would not be distinguishable from the background noise with high statistical confidence. On coarser scales, the northern and tropical land IAV and total (land+ocean) IAV would be robust, but the southern variability and the IAV for the oceans by latitude would not be. These significance results help explain why the published IAV results show little resemblance to each other, except broadly by latitude: these inversions generally used a priori constraints similar to those used here, often with fewer measurements, and so should experience errors at least comparable to those obtained here, with the corresponding lack of significance. What agreement there is occurs only for the regions with the greatest IAV (e.g., Tropical Asia and the East Pacific, two regions that have the most direct response to the largest interannually varying climate driver, the El Niño–Southern Oscillation), for very well-observed regions with somewhat less variability, or else by chance. This generally poor ability to pin down the regional flux IAVs robustly could be improved by either adding more measurement time series, improving the local fidelity of the transport models, or solving for the fluxes at coarser resolution (by assuming more about the spatiotemporal patterns of the flux a priori).

[59] Here we have presented the mean flux IAV results averaged across all 13 models in our sample. If the model-dependent errors cancel out to the extent we have assumed, then these 13-model means IAVs provide substantially more information than the single-model results. Both land and ocean components are at least marginally significant for all three latitude bands. In the northern extratropics, the partition into continents and basins becomes at least marginally significant. Of the 22 emission regions, the IAV for Temperate North America, the South Pacific, Tropical Indian Ocean, and the Northern and Southern Oceans becomes significant.

[60] The key result of our inversion is the attribution of the greater part of the globally observed IAV to the tropical

land regions, especially the release of CO₂ due to the 1997/1998 El Niño and the post-Pinatubo uptake. Half of this variability is robustly attributed to Tropical Asia, with the remainder to Africa/South America. Significant IAV is also obtained in the tropical East Pacific that agrees well with in situ observations. We have found no clear physical mechanisms driving the IAV for the other regions with significant results.

[61] To be able to robustly estimate net flux IAV at scales similar to or finer than the 22 regions examined here, we must both take more measurements in currently under-sampled areas and improve the fidelity of our transport models. Our results suggest that transport model improvements would have the largest impact in the northern extratropics, where there was a fair measurement density already in the 1990s. In the tropics, improving the measurement density is the more urgent problem, particularly around Africa and South America. The dominance of vertical mixing in the tropics suggests that a surface measurement strategy may not be the most productive there: mountain-top sites, aircraft flights, and column-integrated measurements might provide more of a constraint. The potential for using either ¹³C or O₂/N₂ to help partition the land and ocean variability longitudinally is great in the tropics, if certain extra budget terms associated with these additional tracers can be modeled sufficiently well. For the southern extratropics, the lack of the strong vertical motions seen in the tropics suggests that the longitudinal partitioning of flux at the 22-region scale examined here may be achievable with a modest increase in surface measurement sites (the current network, circa 2005, may already be sufficient).

Appendix A: Data Error Specification

[62] Because the data error covariance matrix **R** reflects the errors in $\mathbf{c}_{\text{obs}} - \mathbf{c}_{\text{fwd}}$, it must incorporate errors associated both with the measurement (instrument errors plus errors in the GLOBALVIEW data fitting procedure) and with the modeling of the measurement (including errors in the winds used, in the vertical mixing scheme, in the ability of a transport model to represent the site location, and in the inability of coarse regions and monthly time blocks to correct concentrations at finer scales [Kaminski *et al.*, 2001]). To reflect the fact that this measurement misfit error may vary seasonally and interannually (as measurement techniques change or data density fluctuates), we have based our data errors on a variable part σ_{var} calculated using values from the GLOBALVIEW variability (var) and weight (wts) files, added to a constant part σ_{const} meant to account for the spatial aggregation and representativeness errors, with additional errors σ_{extra} added for a few special sites,

$$\sigma_{\text{data}}^2 = \sigma_{\text{var}}^2 + \sigma_{\text{const}}^2 + \sigma_{\text{extra}}^2. \quad (\text{A1})$$

We use $\sigma_{\text{const}} = 0.30$ ppm, and set $\sigma_{\text{extra}} = 0$ for all time series except KEY_00D0 (2.50 ppm), LJO_04D0 (2.50 ppm), CBA_04D0 (0.90 ppm) PRS_21D0 (0.70 ppm), PRS_21C0 (0.70 ppm), and SEY_00D0 (1.00 ppm for 1988–1996 only). The extra errors on KEY and LJO account for the inability of

our models to properly treat the local flow near cities burning large amounts of fossil fuel. Those for PRS are added to de-weight the two overlapping time series there by $\sim\sqrt{2}$. We have added an extra 1.0 ppm to SEY for 1988–96 (only) because of some likely errors in the data collection procedures there at that time (T. Conway, NOAA/CMDL, personal communication, May 2004) that are not accurately reflected in our data error computation procedure.

[63] Seasonally and interannually varying data uncertainties $\sigma_{\text{var},i}$ for month i are calculated as

$$\sigma_{\text{var},i} = \sigma_{\text{ann}} \frac{\sigma_{\text{seas},i}}{\sigma_{\text{RMS}}^{\text{seas}}} / \sqrt{N_{\text{meas}}}, \quad (\text{A2})$$

where σ_{ann} is the annually resolved residual standard deviation of the individual measurements about the GLOBALVIEW “smooth curve,” taken from the “rsd” column of the GLOBALVIEW “wts” file for the year in question; $\sigma_{\text{seas},i}$ is the monthly resolved standard deviation of the same residuals averaged over all years, taken from the “stdev” column of the GLOBALVIEW “var” file (σ_{ann} being used instead if the number of data points (from the column labeled “#”) used in determining the value for that month is less than 8); $\sigma_{\text{seas}}^{\text{RMS}}$ is the root-mean square of the 12 $\sigma_{\text{seas},i}$ values; and N_{meas} is the effective number of good data values for the month in question. N_{meas} is given by

$$N_{\text{meas}} = \frac{N_{\text{good}} - N_{\text{lost}}}{\gamma + (1 - \gamma) * \beta}, \quad (\text{A3})$$

where N_{good} is the number of measurements available for the month in question; $N_{\text{lost}} = 365/12/40$ accounts for the number of measurements effectively lost because of the use of the “smooth-curve” fit, which has a 40-day window half width; and γ is the number of “weeks” of data available for the month in question, ranging from 0 to 4 and based on the smooth curve values taken from the “S(t)” column of the GLOBALVIEW extended data (ext) file, divided by the number of “weeks” of good data available for the year in question. Finally, N_{good} is approximated as $N_{\text{good}} = N_{\text{good, annual}} * \gamma$, where $N_{\text{good, annual}}$ is the number of good measurements available for the year in question, taken from the “#” column of the GLOBALVIEW “wts” file. The $\gamma + (1 - \gamma)*\beta$ term in the denominator of equation (A3) is meant to increase σ_{var} by $\sqrt{\beta}$ for that portion of the month, $(1 - \gamma)$, for which the interpolated GLOBALVIEW values are used; here we have used $\beta = 2$.

Appendix B: Testing the Significance of the Flux IAV Results With a χ^2 Statistic

[64] We assume that the flux IAV we estimate is composed of a term reflecting the true flux variability of the underlying carbon cycle, as well as a term reflecting the integrated effect of monthly estimation errors and transport errors. To have a useful estimate of the true variability, we would like the true IAV “signal” to be discernible above the “noise” of the random errors, generally with a certain signal-to-noise ratio s (the ratio of the variances of the two signals), say $s \geq 2$.

[65] The significance of the IAV for each estimated time series is tested here using a chi-square statistic,

$$\chi_0^2 = \frac{1}{12} \sum_i \frac{(\mathbf{x}_i^{\text{IAV}} - \mathbf{x}_{i,\text{test}}^{\text{IAV}})^2}{(\sigma_i^{\text{IAV}})^2 + (\text{tr} \sigma_i^{\text{IAV}})^2}, \quad (\text{B1})$$

summing over each month i across 1990–2001 (or $\frac{144}{12} = 12$ years), where σ_i^{IAV} and $\text{tr} \sigma_i^{\text{IAV}}$ are the estimation and transport errors in the estimate of $\mathbf{x}_i^{\text{IAV}}$ described in equations (7) and (9), and where $\mathbf{x}_{\text{test}}^{\text{IAV}}$ is a flux IAV time series to which our estimate is compared. This statistic is the average of 12 separate χ^2 statistics (one for each month, January–December), each one of which measures the variability of \mathbf{x}^{IAV} for the 12 different years. The 12 yearly \mathbf{x}^{IAV} values are assumed to be independent in time for the purposes of this test, as are the estimation and transport errors; this gives the χ^2 statistic $\nu = 12 - 1 = 11$ degrees of freedom.

[66] Using the χ^2 test, we try to reject the null hypothesis that the estimated IAV could have been obtained from a time series with zero underlying IAV ($\mathbf{x}_{\text{test}}^{\text{IAV}} = \mathbf{0}$) but with uncorrelated, Gaussian noise added with a magnitude equal to the root-sum-square (RSS) of the random estimation uncertainty and model transport uncertainty. Using a type I error probability $\alpha = 0.01$ as our threshold, if test probability $P \leq \alpha = 0.01$, then we would reject our hypothesis, meaning that we would believe some other source of variability beyond random estimation error and transport error is present in the time series, which we would take to be the true underlying IAV of the system. The test as outlined above says nothing about how large this true variability must be (it could still be small compared to the noise) but merely that it exists. More broadly, we would like the signal of the true variability to be distinguished above the noise of the background error with some larger signal-to-noise ratio s , say $s \geq 2$. We generalize the test here to determine whether true underlying variability is present with a given signal-to-noise ratio by increasing the variance of the noisy test time series by a factor of $1 + s^2$. In statistical terms, the signal-to-noise ratio s is the ratio of variances of the estimated IAV time series to the estimated noise (the RSS of the transport and random estimation uncertainties).

[67] In Figures 2 and 4–8, we plot the 1σ intermodel spread $\text{tr} \sigma_i^{\text{IAV}}$ as a proxy for transport error, as well as the RMS of the 1σ estimation error σ_i^{IAV} across all 13 models. These errors characterize those we would expect for any one model in our set of 13. We would expect the errors on our 13-model mean results to be smaller, however, by as much as a factor of $\sqrt{13}$ if the errors from each model were completely independent. We know that our models are not completely independent, though: We have three versions of MATCH and two versions of the GISS model in our set, for example, and many of the models use similar winds, and vertical mixing schemes. Also, that portion of the data error (the mismatch between the true measurements and the model-dependent estimate) that is not dependent on the transport model used, the instrument error and the error caused by using flux corrections over large regions to try to fit multiple measurement time series, represented here by σ_{const} in equation (A1), will not be reduced by averaging across models. To account for this poorly known error reduction, we define a parameter

N_{ind} representing the number of independent models in our 13-model set (such that the 13-model mean errors are reduced by a factor of $\sqrt{N_{\text{ind}}}$ over the single-model errors) and give significance results for different values of it.

[68] The χ_0^2 values from equation (B1) could be used to test the χ^2 significance of the results of any one of our models ($N_{\text{ind}} = 1$) at the minimal ($s = 0$) signal-to-noise ratio. To test the significance of the 13-model mean results at any desired signal-to-noise ratio s , however, these χ_0^2 values must be multiplied by a factor $N_{\text{ind}}/(1 + s^2)$. Table 4 gives the basic ($N_{\text{ind}} = 1, s = 0$) χ_0^2 value for each region, plus the probability that the null hypothesis is true for various values of $\chi_{\text{mean}}^2(s) = \frac{N_{\text{ind}}}{1+s^2} \chi_0^2$. To test the significance of the fluxes for any single model in the set ($N_{\text{ind}} = 1$) at a signal-to-noise ratio of $s = 2$, for example, the $N_{\text{ind}}/(1 + s^2) = 0.2$ column should be used. In discussing the 13-model mean flux IAV results in the text, we test their significance at the $s = 2$ level assuming an error reduction given by $N_{\text{ind}} = 5$, using the $N_{\text{ind}}/(1 + s^2) = 1.0$ column. The choice to use $N_{\text{ind}} = 5$ is subjective; we choose it here as a midrange value.

[69] Here, a flux time series' IAV is considered “significant” if the test probability $P \leq 0.01$, “marginally significant” for $P = 0.01 - 0.05$, and “not significant” for $P \geq 0.05$. Test probabilities P for each 13-model mean flux IAV time series are given in the $N_{\text{ind}}/(1 + s^2) = 1.0$ column of Table 4. At these levels, we should expect to make the (type I) error of incorrectly calling the IAV “significant” or “marginally significant” when it really is not only 5% of the time, or for about one of the 22 emission regions (for only one of the nine regions significant at this level in Table 4). Of course, by choosing this relatively stringent level for significance, we increase our risk of making a type II error [Sokal and Rohlf, 1969]: calling the low IAVs for certain regions ‘not significant’, when in fact they are. We choose to accept this higher level of type II errors for low-IAV regions, since our focus is on assessing the robustness of the high-IAV regions.

[70] **Acknowledgments.** This work was made possible through support from the National Science Foundation (OCE-9900310), the National Oceanic and Atmospheric Administration (NA67RJ0152, Amendment 30), the International Geosphere Biosphere Program/Global Analysis, Interpretation, and Modeling Project, and the Global Carbon Project. D. F. B. would like to thank NASA's Graduate Student Researchers Program, NOAA's Office of Global Programs, and Jorge Sarmiento and the Carbon Modeling Consortium for support while at Princeton University, and the Advanced Studies Program for support at NCAR. K. R. G. and A. S. D. were supported by NASA Cooperative Agreement NCC5-621. We thank all the scientists who have collected and contributed CO₂ data to the GLOBALVIEW-CO₂ database, as well as those at NOAA/CMDL who support it, including Pieter Tans and Tom Conway. We also thank Ian Enting, Prabir Patra, Cathy Trudinger, Andy Jacobson, and Cindy Nevison for their helpful comments.

References

- Andres, R. J., G. Marland, I. Fung, and E. Matthews (1996), A $1^\circ \times 1^\circ$ distribution of carbon dioxide emissions from fossil fuel consumption and cement manufacture, 1950–1990, *Global Biogeochem. Cycles*, *10*, 419–429.
- Baker, D. F. (1999), An inversion method for determining time-dependent surface CO₂ fluxes, in *Inverse Methods in Global Biogeochemical Cycles*, *Geophys. Monogr.*, vol. 114, edited by P. Kasibhatla et al., pp. 279–293, AGU, Washington, D. C.
- Baker, D. F. (2001), Sources and sinks of atmospheric CO₂ estimated from batch least squares inversions of CO₂ concentration measurements, Ph.D. dissertation, 414 pp., Program in Atmos. and Oceanic Sci., Princeton Univ., Princeton, N. J.

- Bousquet, P., P. Peylin, P. Ciais, C. Le Quééré, P. Friedlingstein, and P. Tans (2000), Regional changes in carbon dioxide fluxes of land and oceans since 1980, *Science*, *290*, 1342–1346.
- Dargaville, R. J., R. M. Law, and F. Pribac (2000), Implications of interannual variability in atmospheric circulation on modeled CO₂ concentrations and source estimates, *Global Biogeochem. Cycles*, *14*, 931–943.
- Energy Information Administration (2002), U.S. Department of Energy, Table H.1: World carbon dioxide emissions from the consumption and flaring of fossil fuels, 1980–present, *Int. Energy Annu.*, 2002. (Available at <http://www.eia.doe.gov/emeu/ica/tableh1.html>)
- Enting, I. (2002), *Inverse Problems in Atmospheric Constituent Transport*, Cambridge Univ. Press, New York.
- Feely, R. A., et al. (2002), Seasonal and interannual variability of CO₂ in the equatorial Pacific, *Deep Sea Res., Part II*, *49*, 2443–2469.
- GLOBALVIEW-CO₂ (2004), *Cooperative Atmospheric Data Integration Project—Carbon Dioxide [CD-ROM]*, Natl. Oceanic and Atmos. Admin., Clim. Modell. and Diag. Lab. (CMDL), Boulder, Colo. (Available via anonymous FTP at <ftp.cmdl.noaa.gov>, Path: [cg/co2/GLOBALVIEW](ftp://ftp.cmdl.noaa.gov/path/cg/co2/GLOBALVIEW))
- Gurney, K. R. (2004), Towards robust regional estimates of carbon sources and sinks using atmospheric transport models, Ph.D. dissertation, Grad. Degree Program in Ecol., Colo. State Univ., Fort Collins.
- Gurney, K. R., et al. (2002), Towards robust regional estimates of CO₂ sources and sinks using atmospheric transport models, *Nature*, *415*, 626–630.
- Gurney, K. R., et al. (2003), Transcom 3 CO₂ inversion intercomparison: 1. Annual mean control results and sensitivity to transport and prior flux information, *Tellus, Ser. B*, *55*, 555–579.
- Gurney, K. R., et al. (2004), Transcom 3 inversion intercomparison: Model mean results for the estimation of seasonal carbon sources and sinks, *Global Biogeochem. Cycles*, *18*, GB1010, doi:10.1029/2003GB002111.
- Kaminski, T., P. J. Rayner, M. Heimann, and I. G. Enting (2001), On aggregation errors in atmospheric transport inversions, *J. Geophys. Res.*, *106*(D5), 4703–4715.
- Keeling, C. D., R. B. Barcastow, A. F. Carter, S. C. Piper, T. P. Whorf, M. Heimann, W. G. Mook, and H. Roeloffzen (1989), A three-dimensional model of atmospheric CO₂ transport based on observed winds: 1. Analysis of observational data, in *Aspects of Climate Variability in the Pacific and the Western Americas*, *Geophys. Monogr. Ser.*, vol. 55, edited by D. H. Peterson, pp. 165–236, AGU, Washington, D. C.
- Langenfelds, R. L., R. J. Francey, B. C. Pak, L. P. Steele, J. Lloyd, C. M. Trudinger, and C. E. Allison (2002), Interannual growth rate variations of atmospheric CO₂ and its ¹³C, H₂, CH₄, and CO between 1992 and 1999 linked to biomass burning, *Global Biogeochem. Cycles*, *16*(3), 1048, doi:10.1029/2001GB001466.
- Law, R. M. (1999), CO₂ sources from a mass-balance inversion: Sensitivity to the surface constraint, *Tellus, Ser. B*, *51*, 254–265.
- Law, R. M., Y.-H. Chen, K. R. Gurney, and TransCom 3 modelers (2003), TransCom 3 CO₂ inversion intercomparison: 2. Sensitivity of annual mean results to data choices, *Tellus, Ser. B*, *55*, 580–595.
- Marland, G., T. A. Boden, and R. J. Andres (2003), Global, regional, and national CO₂ emissions, in *Trends: A Compendium of Data on Global Change*, pp. 505–584, Carbon Dioxide Inf. Anal. Cent., Oak Ridge Natl. Lab., U.S. Dep. of Energy, Oak Ridge, Tenn. (Available at http://cdiac.esd.ornl.gov/trends/emis/tre_glob.htm)
- Masarie, K. A., and P. P. Tans (1995), Extension and integration of atmospheric carbon dioxide data into a globally consistent measurement record, *J. Geophys. Res.*, *100*(D6), 11,593–11,610.
- Murayama, S., S. Taguchi, and K. Higuchi (2004), Interannual variation in the atmospheric CO₂ growth rate: Role of atmospheric transport in the Northern Hemisphere, *J. Geophys. Res.*, *109*, D02305, doi:10.1029/2003JD003729.
- Page, S. E., F. Siegert, J. O. Rieley, H. D. V. Boehm, A. Jaya, and S. Limin (2002), The amount of carbon released from peat and forest fires in Indonesia during 1997, *Nature*, *420*, 61–65.
- Peylin, P., D. Baker, J. Sarmiento, P. Ciais, and P. Bousquet (2002), Influence of transport uncertainty on annual mean and seasonal inversions of atmospheric CO₂ data, *J. Geophys. Res.*, *107*(D19), 4385, doi:10.1029/2001JD000857.
- Peylin, P., P. Bousquet, C. Le Quééré, S. Sitch, P. Friedlingstein, G. McKinley, N. Gruber, P. Rayner, and P. Ciais (2005), Multiple constraints on regional CO₂ flux variations over land and oceans, *Global Biogeochem. Cycles*, *19*, GB1011, doi:10.1029/2003GB002214.
- Piper, S. C., C. D. Keeling, M. Heimann, and E. F. Stewart (2001a), Exchanges of atmospheric CO₂ and ¹³CO₂ with the terrestrial biosphere and oceans from 1978 to 2000: II. A three-dimensional tracer inversion model to deduce regional fluxes, *SIO Ref. 01-07*, Scripps Inst. of Oceanogr., Univ. of Calif., San Diego, La Jolla.
- Piper, S. C., C. D. Keeling, and E. F. Stewart (2001b), Exchanges of atmospheric CO₂ and ¹³CO₂ with the terrestrial biosphere and oceans from 1978 to 2000: III. Sensitivity tests, *SIO Ref. 01-08*, Scripps Inst. of Oceanogr., Univ. of Calif., San Diego, La Jolla.
- Prentice, I. C., G. D. Farquhar, M. J. R. Fasham, M. L. Goulden, M. Heimann, V. J. Jaramillo, H. S. Khesghi, and C. Le Quééré (2001), The carbon cycle and atmospheric carbon dioxide, in *Climate Change 2001: The Scientific Basis, Contribution of Working Group I to the Third Assessment Report of the Intergovernmental Panel on Climate Change*, edited by J. T. Houghton et al., pp. 183–287, Cambridge Univ. Press, New York.
- Randerson, J. T., M. V. Thompson, T. J. Conway, I. Y. Fung, and C. B. Field (1997), The contribution of terrestrial sources and sinks to trends in the seasonal cycle of atmospheric carbon dioxide, *Global Biogeochem. Cycles*, *11*, 535–560.
- Rayner, P. J., I. G. Enting, R. J. Francey, and R. L. Langenfelds (1999), Reconstructing the recent carbon cycle from atmospheric CO₂, δ¹³C and O₂/N₂ observations, *Tellus, Ser. B*, *51*, 213–232.
- Rödenbeck, C., S. Houweling, M. Gloor, and M. Heimann (2003), CO₂ flux history 1982–2001 inferred from atmospheric data using a global inversion of atmospheric transport, *Atmos. Chem. Phys.*, *3*, 1919–1964.
- Sokal, R. R., and F. J. Rohlf (1969), *Biometry: The Principles and Practice of Statistics in Biological Research*, 776 pp., W. H. Freeman, New York.
- Takahashi, T., R. H. Wanninkhof, R. A. Feely, R. F. Weiss, D. W. Chipman, N. Bates, J. Olafsson, C. Sabine, and S. C. Sutherland (1999), Net sea-air CO₂ flux over the global oceans: An improved estimate based on the sea-air pCO₂ difference, in *Proceedings of the 2nd International Symposium: CO₂ in the Oceans, the 12th Global Environmental Tsukuba, 18–22 January 1999*, *Tsukuba Center of Institutes*, edited by Y. Nojiri, Natl. Inst. for Environ. Stud., Environ. Agency of Jpn., Tokyo.
- D. F. Baker, Climate and Global Dynamics Division, National Center for Atmospheric Research, 1850 Table Mesa Drive, Boulder, CO 80305, USA. (dfb@ucar.edu)
- P. Bousquet, P. Ciais, P. Peylin, and P. J. Rayner, Laboratoire des Sciences du Climat et de l'Environnement, F-91198 Gif-sur-Yvette, France. (bousquet@lscce.saclay.cea.fr; ciais@lscce.saclay.cea.fr; peylin@lscce.saclay.cea.fr; peter.rayner@cea.fr)
- L. Bruhwiler and K. Masarie, Climate Monitoring and Diagnostics Laboratory, National Oceanic and Atmospheric Administration, 326 Broadway R/CG1, Boulder, CO 80303, USA. (lori.bruhwiler@noaa.gov; kenneth.masarie@noaa.gov)
- Y.-H. Chen, Department of Earth, Atmospheric, and Planetary Sciences, Massachusetts Institute of Technology, 77 Massachusetts Avenue, Cambridge, MA 02139-4307, USA. (didi@mit.edu)
- A. S. Denning, Department of Atmospheric Science, Colorado State University, Fort Collins, CO 80523, USA. (denning@atmos.colostate.edu)
- I. Y. Fung and J. John, Center for Atmospheric Sciences, University of California, Berkeley, 399 McCone Hall, Berkeley, CA 94720-4767, USA. (ifung@uclink4.berkeley.edu; jasmmin@atmos.berkeley.edu)
- K. R. Gurney, Department of Earth and Atmospheric Sciences and Department of Agronomy, Purdue University, 550 Stadium Mall Drive, West Lafayette, IN 47907-2051, USA. (keving@atmos.colostate.edu)
- M. Heimann, Department of Biogeochemical Systems, Max-Planck-Institut für Biogeochemie, P. O. Box 100164, D-07701 Jena, Germany. (martin.heimann@bgc.jena.mpg.de)
- R. M. Law and B. N. Pak, CSIRO Marine and Atmospheric Research, PMB 1, Aspendale, Victoria 3195, Australia. (rachel.law@csiro.au; bernard.pak@csiro.au)
- T. Maki, Quality Assurance Section, Atmospheric Environment Division, Observations Department, Japan Meteorological Agency, 1-3-4 Otemachi, Chiyoda-ku, Tokyo 100-8122, Japan. (maki@met.kishou.go.jp)
- S. Maksyutov, Institute for Global Change Research, Frontier Research Center for Global Change, Japan Agency for Marine-Earth Science and Technology, Yokohama 236-0001, Japan. (shamil@jamstec.go.jp)
- M. Prather, Department of Earth System Science, University of California, Irvine, 3329 Croul Hall, Irvine, CA 92697-3100, USA. (mprather@uci.edu)
- S. Taguchi, Global Environment Study Group, Research Institute of Environmental Management Technology, National Institute of Advanced Industrial Science and Technology, AIST-WEST, 16-1 Onogawa, Tsukuba, Ibaraki 305-8569, Japan. (s.taguchi@aist.go.jp)
- Z. Zhu, Science Systems and Applications, Inc., 10210 Greenbelt Road, Suite 600, Lanham, MD 20706, USA. (zhu@mulan.gsfc.nasa.gov)